

Volume, heat, and freshwater transports of the global ocean circulation 1993–2000, estimated from a general circulation model constrained by World Ocean Circulation Experiment (WOCE) data

D. Stammer,¹ C. Wunsch,² R. Giering,³ C. Eckert,² P. Heimbach,² J. Marotzke,⁴
A. Adcroft,² C. N. Hill,² and J. Marshall²

Received 27 August 2001; revised 29 April 2002; accepted 15 August 2002; published 4 January 2003.

[1] An analysis of ocean volume, heat, and freshwater transports from a fully constrained general circulation model (GCM) is described. Output from a data synthesis, or state estimation, method is used by which the model was forced to large-scale, time-varying global ocean data sets over 1993 through 2000. Time-mean horizontal transports, estimated from this fully time-dependent circulation, have converged with independent time-independent estimates from box inversions over most parts of the world ocean but especially in the southern hemisphere. However, heat transport estimates differ substantially in the North Atlantic where our estimates result in only 1/2 previous results. The models drift over the estimation period is consistent with observations from TOPEX/Poseidon in their spatial pattern, but smaller in their amplitudes by about a factor of 2. Associated temperature and salinity changes are complex, and both point toward air–sea interaction over water mass formation regions as the primary source for changes in the deep ocean. The estimated mean circulation around Australia involves a net volume transport of 11 Sv through the Indonesian Throughflow and the Mozambique Channel. In addition, we show that this flow regime exists on all timescales above 1 month, rendering the variability in the South Pacific strongly coupled to the Indian Ocean. Moreover, the dynamically consistent variations in the model show temporal variability of oceanic heat transports, heat storage, and atmospheric exchanges that are complex and with a strong dependence upon location, depth, and timescale. Our results demonstrate the great potential of an ocean state estimation system to provide a dynamical description of the time-dependent observed heat transport and heat content changes and their relation to air–sea interactions.

INDEX TERMS: 4532 Oceanography: Physical: General circulation; 4504 Oceanography: Physical: Air/sea interactions (0312); 4294 Oceanography: General: Instruments and techniques; 4556 Oceanography: Physical: Sea level variations; 4842 Oceanography: Biological and Chemical: Modeling;
KEYWORDS: ocean circulation, data assimilation, heat transport, surface fluxes, ocean reanalysis

Citation: Stammer, D., C. Wunsch, R. Giering, C. Eckert, P. Heimbach, J. Marotzke, A. Adcroft, C. N. Hill, and J. Marshall, Volume, heat, and freshwater transports of the global ocean circulation 1993–2000, estimated from a general circulation model constrained by World Ocean Circulation Experiment (WOCE) data, *J. Geophys. Res.*, 108(C1), 3007, doi:10.1029/2001JC001115, 2003.

1. Introduction

[2] One of the primary purposes of the World Ocean Circulation Experiment (WOCE) has been to determine and understand the general circulation and its transport variability over an extended period of time. This goal can be achieved by

bringing a full ocean circulation model into consistency with the available, diverse, in situ and satellite observations, and by then using the resulting synthesis/estimates to study a variety of phenomena. Among them are, the circulation, its energetics, driving forces, property fluxes, dynamical balances, ventilation and mixing, and the nature and structure of its variability, among many other problems.

[3] In a previous paper [Stammer *et al.*, 2002a, herein after referred to as Paper 1], we described such a synthesis obtained by combining a general circulation model (GCM) with much of the existing global WOCE data set from a six year interval 1992–1997, in a procedure called “state estimation” or “data assimilation.” In contrast to a number of other synthesis efforts [e.g., Carton *et al.*, 2000a, 2000b], a deliberate decision was made to use a general method that could become increasingly rigorous as computer power

¹Physical Oceanography Research Division, Scripps Institution of Oceanography, University of California, San Diego, La Jolla, California, USA.

²Massachusetts Institute of Technology, Cambridge, Massachusetts, USA.

³FastOpt, GBR, Hamburg, Germany.

⁴Southampton Oceanography Centre, University of Southampton, Southampton, UK.

grows and as knowledge of the underlying statistics improves. The price paid is a significantly greater computational load. In Paper 1 we provide some general tests of the adequacy of the model-data combination. In particular, the

paper shows that the constrained model displays considerable skill in reproducing both the constraining observations and much of the withheld data. Remaining discrepancies can lie with either the model, the data, or both, and require further information to resolve.

[4] Despite various lingering issues, we will begin here to exploit for scientific purposes the estimation results shown in Paper 1. The focus will be on the determination of the ocean horizontal transports of volume, heat and freshwater and their divergences that appear to be most important to understanding the climate system. Results are obtained by analyzing a new calculation that was extended from the previous six-year estimation period to a total of nine years from 1992 through 2000 and by including extra constraints to prevent model drift. Otherwise, the configuration is as described in Paper 1. A detailed analysis of associated surface heat, freshwater, and momentum fluxes and their uncertainties are described by D. Stammer et al. (Improving air-sea flux estimates through global ocean data assimilation, submitted for publication, 2002b, hereinafter referred to as Stammer et al., submitted manuscript, 2002b). Obtaining realistic oceanic property transports, such as those for temperature, puts stringent demands on a model: the transports are second-order quantities, involving products of velocities and property distributions; models that produce sensible-appearing flow and temperature fields may well fail to estimate accurately integrated products of these fields.

[5] We will first describe the time average results. But because of: (1) the nature of the imposed altimetric data set which best constrains the time variability in our solution on timescales out to about a decade (details about the data used as constraints are provided below), and (2) concerns about the adequacy of our model resolution, we believe that the temporal variability of properties in our results is considerably more accurate than is the time average or absolute values. Most of our subsequent emphasis will therefore be on the temporally fluctuating components. The results reported are believed to be the first obtained from an analysis in which consistency has been achieved with both dynamics and observations. More applications of the estimated ocean state exist than the one described here; for example, *Ponte et al.* [2001], used the same results to study the Earth's angular momentum balance, and efforts to calculate biogeochemical fluxes are underway.

[6] In the absence so far (owing to the associated computational demand) of a formal error analysis of the estimated ocean state, comparisons with independent estimates of various quantities were used in Paper 1 to build up an empirical depiction of the overall accuracy of the results. One example of the skill of the present analysis can

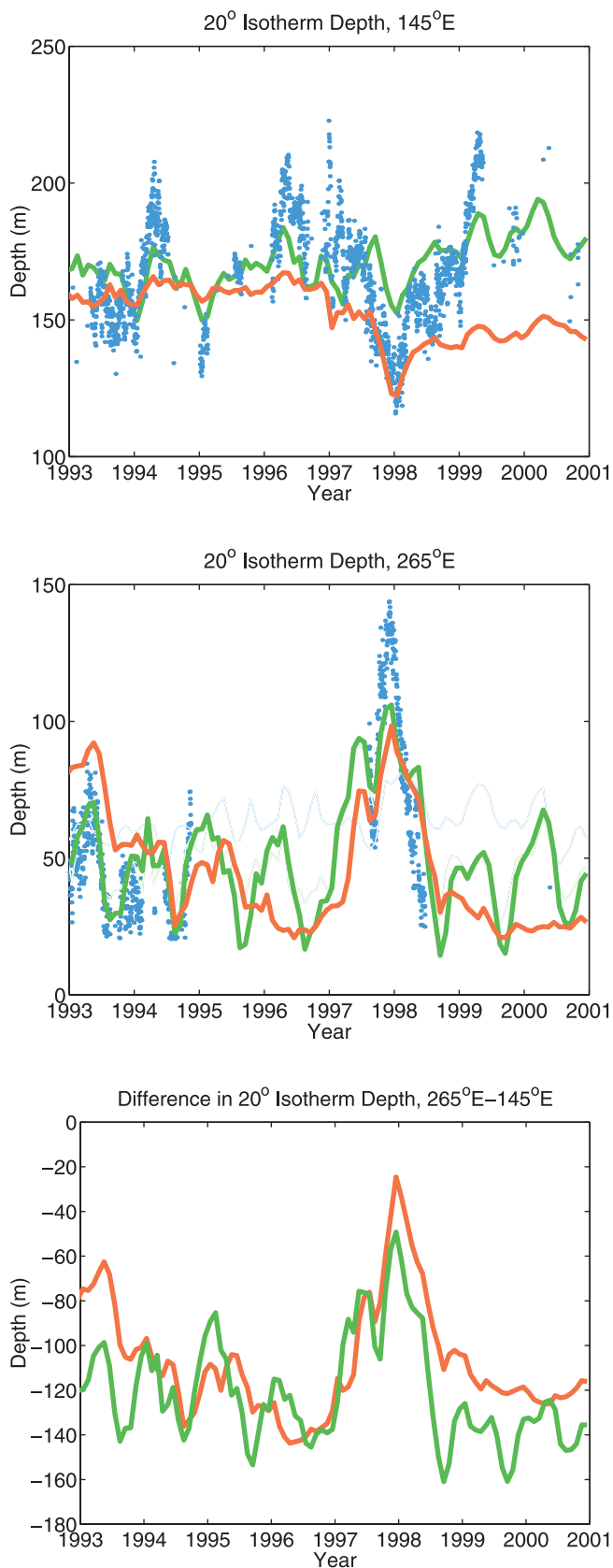


Figure 1. (opposite) (top) Depth of 20° isotherm as a function of time evaluated from TOGA-TAO data from 140° to 150° E on the equator (blue dots). Red and green curves are estimates at the same location obtained from the unconstrained and constrained model runs, respectively. (middle) Same as top panel, but from 265° E on the equator. (bottom) Zonal difference in the depth of the 20° isotherm, evaluated from the unconstrained (red) and constrained model (green), respectively. Here and in all other respective figures, year numbers mark the beginning of the calendar years.

be found in Figure 1 which depicts the monthly mean estimated depth of the 20°C isotherm together with observations from TOGA-TAO (Tropical Ocean Global Atmosphere-Tropical Atmosphere-Ocean) buoys [McPhaden *et al.*, 1998] on the equator between 140°–150°E and at 265°E; these data were not used as constraints. In contrast to the discontinuous TAO measurements, the constrained model simulates the isotherm depth continuously over the full estimation period. It tracks the data where they exist and allows one to infer changes and their dynamics even when data are absent.

[7] The results in the figure are noteworthy given the low resolution of the model, and because the time-varying signal is prescribed essentially only through the NCEP surface forcing and the altimetric observations. Although none of the TAO or expendable bathythermograph (XBT) data were used to constrain the model, one sees the clear signal of the 1992/1993, 1994/1995, and especially the 1997/1998 El Niño events in the depth of the 20° isotherm. Moreover, those three ENSO events show up as substantially reduced east–west slopes in the isotherm, followed by a rapid reversal of this tendency during the subsequent build-up phase in the constrained system. As compared to the estimate, the unconstrained model produces a fairly constant isotherm depth in the west during the first few years. It seems to capture the last ENSO event surprisingly well, but stays biased shallow subsequently at the western side of the basin. In the east, the depth is too great during the first years and again tends to become too shallow toward the end. Moreover, the unconstrained model does not simulate the detailed oscillations in the east–west thermocline slope.

[8] The mean depths of the 20°C isotherms are displayed in Figure 2 over the global model domain. Outcrops clearly reflect the advection of water by the mean circulation, i.e., the flux of warm water northward by the western boundary currents and the equatorward flow of cold water on the eastern side of the basins. The southern parts of the subtropical gyres are prominent, showing the maximum isotherm depths. Also depicted are the time-mean depths for the 10°C and 4°C isotherms. For the 10°C isotherm, the gyre signatures are again conspicuous, as are ventilation “windows” at the eastern side of the basins. In contrast, the depth of the 4°C isotherm points toward water mass formation sites, such as the Mediterranean, the Red and Okhotsk Seas, where unusually warm or cold water masses emerge into the large-scale circulation.

[9] Section 2 provides a brief summary of the estimation system and model. Section 3 addresses transients and drift in the model solution, and their potential implications. Section 4 describes the estimated time-mean transports of volume, heat and freshwater, as well as the relation of the latter two to surface flux fields. Time-dependent volume transports; the dynamics and kinematics of transient heat transports are discussed in sections 5 and 6. Formal computation of regional heat content changes and their relationship to lateral and vertical transport processes and surface forcing are found in section 7.

2. Methodology and Model Set-Up

[10] Paper 1 provides a full account of the state estimation method (Lagrange multipliers, or adjoint) and the general

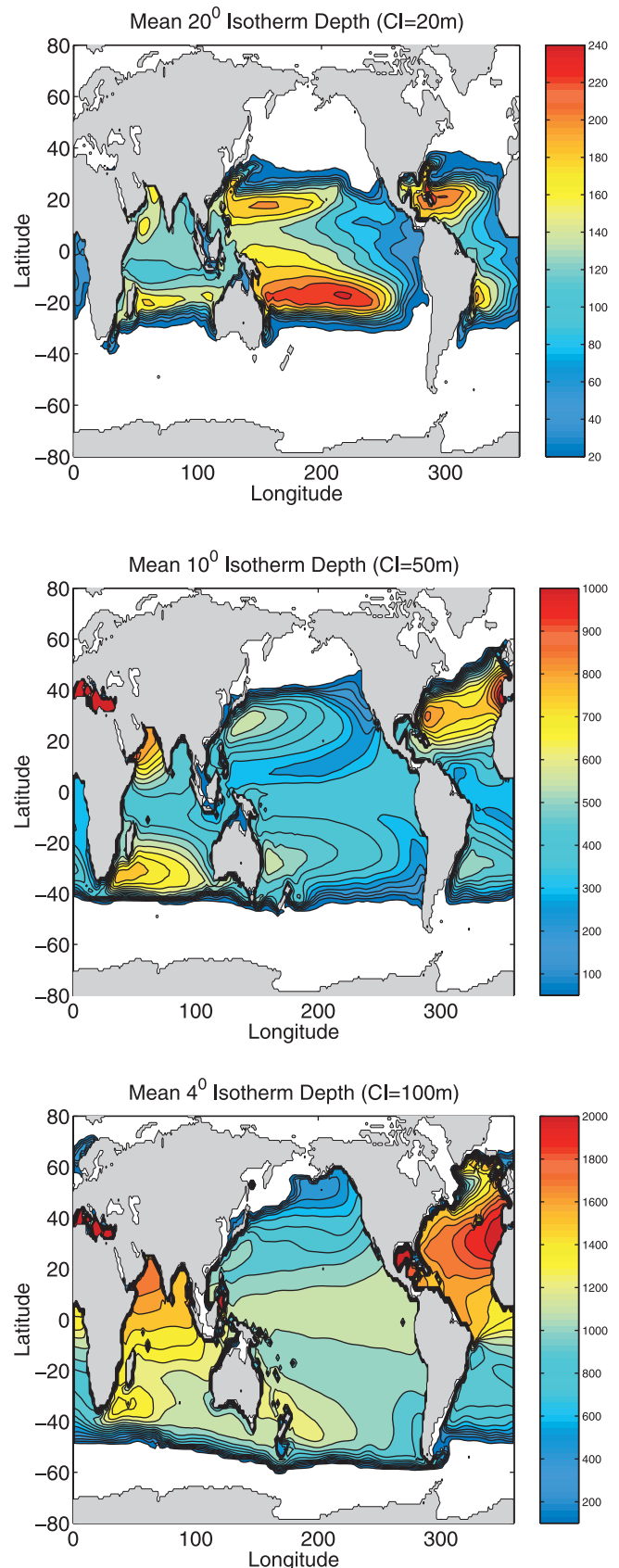


Figure 2. (top) Mean depths of the 20°C isotherm. The contour interval is 20 m. (middle) The depth of the 10°C isotherm and (bottom) the 4°C isotherm with contour increments of 50 and 100 m, respectively.

model configuration. All estimates are based on the ocean general circulation model (GCM) [Marshall *et al.*, 1997a, 1997b] and its adjoint [Marotzke *et al.*, 1999], which have been developed at the Massachusetts Institute of Technology. This model uses the primitive equations on a sphere under the Boussinesq approximation. It consists of prognostic equations for horizontal velocity, heat, and salt, and an equation of state that are integrated forward in time on a staggered “C-grid” [Arakawa and Lamb, 1977]. Spatial coordinates are longitude, latitude, and height. For present purposes, we use a hydrostatic version with an implicit free-surface. A full surface mixed layer model is used (called “KPP” [Large *et al.*, 1994]) in the forward and adjoint model. Underneath the surface mixed layer, convective adjustment is used to remove gravitational instabilities.

[11] The GCM is configured globally with 2° horizontal resolution over $\pm 80^\circ$ in latitude with 22 levels in the vertical. Laplacian viscosity and diffusivities are used, with $\nu_h = 5 \times 10^4$ and $\kappa_h = 10^3$ and $\nu_v = 10^{-3}$ and $\kappa_v = 10^{-5}$, in the horizontal and vertical respectively, with free-slip bottom, and nonslip lateral wall boundary conditions. To allow a time step of one hour, an implicit scheme was used for the vertical mixing. Near the sea surface, the vertical coefficients specified by the KPP model can be higher by an order of magnitude or more than those of the background values.

[12] Constraining data include both mean and time-varying altimetry from TOPEX/Poseidon and the ERS-1/2 satellites, the *Levitus et al.* [1994a, 1994b] monthly hydrographic climatologies over the full water column, monthly mean surface temperature fields, as well as the estimated air–sea fluxes of momentum (twice/day), fresh water and heat from daily atmospheric estimates. Descriptions of the relative weights specified for each of those data sets are provided in Paper 1. Note that SST fields received a relatively low weight owing to lingering problems with the model mixed layer formulation.

[13] Approximate initial conditions were obtained from the *Levitus et al.* [1994a, 1994b] January potential temperature and salinity fields. In the present calculation, the control parameters include adjustments to the initial-condition potential temperature, θ , and salinity, S , fields, as well as the daily surface momentum, heat and freshwater fluxes over the full nine years. That is, we assume that the model uncertainties reside entirely in the initial conditions and first guess surface forcing fields. The latter are obtained from the National Center for Environmental Prediction (NCEP)/National Center for Atmospheric Research (NCAR) reanalysis project products [Kalnay *et al.*, 1996]. In the present configuration, virtual salt fluxes are used instead of freshwater. No river run-off was present explicitly, nor is the salt flux out of the Mediterranean represented accurately; the estimation procedure corrects this deficiency by changing the surface freshwater fluxes accordingly (see also Stammer *et al.*, submitted manuscript, 2002b).

[14] The basis of this analysis is a final calculation from the forward model that starts from the estimated initial-conditions for temperature and salinity, and that is driven by the optimized surface forcing fields. This estimated state is thus consistent with the data within the uncertainties described above, and simultaneously is a solution to a freely running GCM. From that computation, five-day averages of horizontal transports and monthly means of the full model

state were stored for a further analysis, including in some cases, further reduction to 30-day averages (see also <http://www.ecco-group.org/las>).

3. Trends and Transients

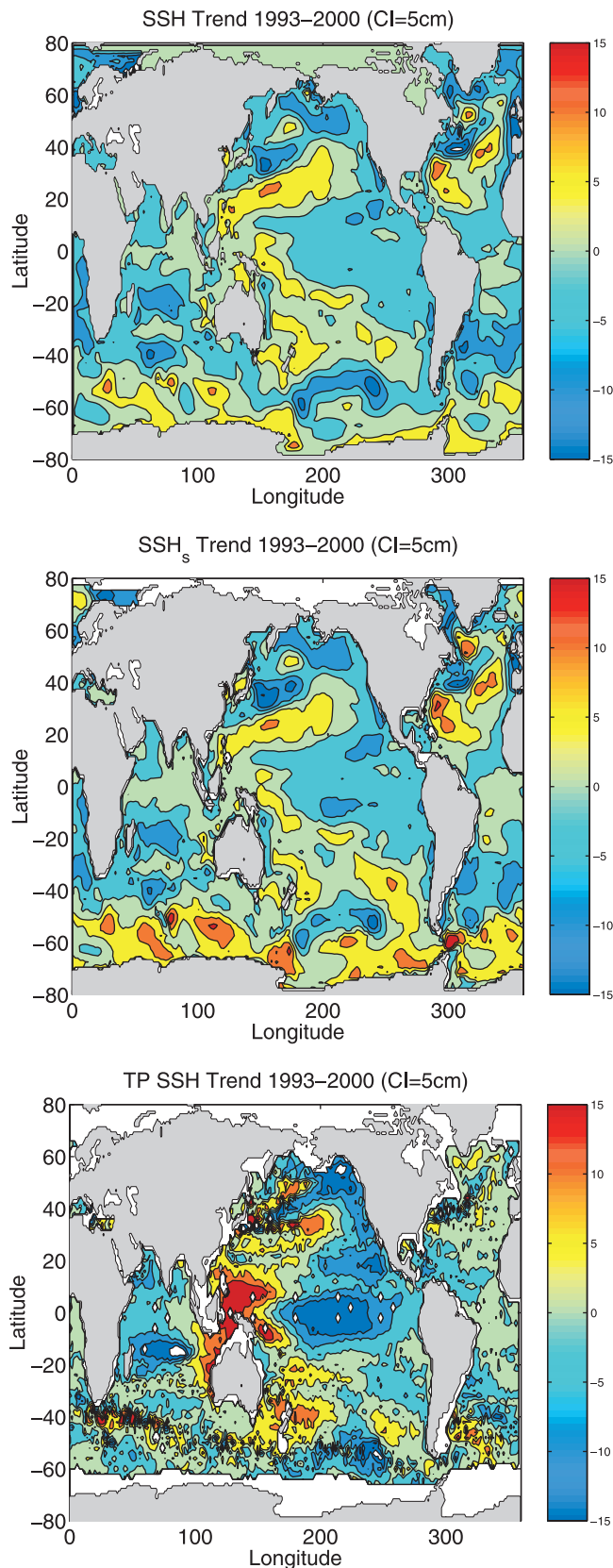
[15] Changes in the temperature and salinity initial conditions and surface fluxes are estimated so that the model-data misfit and the model drift are both minimized over the entire period. Constraining the model drift speeded up the surface flux adjustments during the optimization. This constraint was imposed by requiring that the first and last year do not differ in temperature and salinity by more than 10% of the estimated uncertainty at all points. (These constraints are equivalent to asserting that observations show that the ocean does not drift significantly over a decade, although as we discuss below, the inference is not a very firm one.) Because the estimated changes in initial conditions are not dynamically consistent with geostrophy, the model does show initial transients. Prominent effects are associated with an enhanced bottom torque and related large vertical velocities near steep topography. However, these features largely disappeared after the first year, and only the remaining eight years are used for further analysis. In future calculations, a dynamical constraint on the changes of initial conditions will be imposed to minimize the bottom torque term.

[16] Although small, regional drifts of the model sea surface height, temperature and salinity fields are not eliminated altogether. The model adjustment is displayed in Figure 3a showing the global distribution of changes in sea surface height, 1993–2000, estimated by least squares fitting a straight line over the interval. The largest changes are of the order of ± 15 cm and can be found in the subpolar regions of both hemispheres. Smaller changes are visible in the tropical and subtropical oceans. All these changes show intriguing gyre or circulation structures. Sea surface height changes along two positive ridges across the Pacific in both hemispheres. A somewhat similar structure seems to be present also in the North Atlantic.

[17] To compare the estimated sea surface height (SSH) drift with observations, we show in the lower panel of the figure (Figure 3) estimates from the same eight years of TOPEX/POSEISON altimeter data. In many locations, these altimeter-alone fields are similar to those estimated by the data/model combination, but they do show substantially larger amplitudes, suggesting that the drift of the physical ocean state may have been too firmly suppressed in the model. Most changes in the model can be explained by the steric (density) shifts (Figure 3b), but some fraction cannot be explained by the steric change and is due to mass redistribution. This is most notable over the Southern Ocean. The implied density shifts are discussed in more detail later. The resulting mean meridional transport imbalance can be obtained by integrating the models meridional flow zonally around the entire globe (not shown). Those results suggest volume shifts of the order of 10^{-3} Sv, a difficult value to observe.

[18] The agreement between the model and TOPEX/Poseidon data [see also *Nerem et al.*, 1999; F. Condi, personal communication, 2000] demonstrate one of the fundamental difficulties encountered in explaining global and regional change in sea surface height and subsurface

temperature or salinity in the presence of numerical model drift. Separating real physical shifts from regional numerical drift will be a challenge for long-term climate simulations and observations.



[19] Ideally a climate-oriented ocean state estimation system should provide estimates not just the flow field, but also of quantities such as global sea level changes. For that purpose two important extensions will be required: (1) the model needs to be truly global and then needs to include an ice model. (2) The Boussinesq approximation renders the numerical model currently used as volume rather than mass conserving. To properly simulate global changes in sea level one needs to remove this approximation. This step is also important for studies of the Earth's changing mass field and the role the ocean plays in the overall mass balance.

4. Time-Mean Volume, Heat, and Freshwater Transports

4.1. Volume Fluxes

[20] The horizontal transport of volume across an ocean basin of width L , and depth $h(x)$, is defined conventionally as,

$$H_V(t) = \int_0^L \int_{-h(x)}^0 v(x, z, t) dz dx, \quad (1)$$

where v is the velocity component normal to a cross-basin section. In Figure 4a, we show the time-mean and temporal standard deviation of H_V across several sections that coincide with nominal WOCE one-time hydrographic sections. Because the underlying MIT GCM uses the Boussinesq approximation, volume transport is the appropriate surrogate for mass movement. The northern model boundary is closed-resulting in no net volume exchange across the Arctic, and so mean meridional volume fluxes in the Northern Hemisphere are zero. The few available estimates of the flux into the Arctic [e.g., *Roach et al., 1995*] suggest that less than 1 Sv is involved; it will be included in future computations.

[21] In contrast to enclosed basins, closed flow loops do show net fluxes. The most conspicuous such loop is the anticyclonic circulation around Australia, where a time-mean total of about 11 Sv flows northward in the South Pacific, through the Indonesian Throughflow, and returns southward through the Mozambique Channel. East of Madagascar about 5 Sv are flowing northward across 20°S in the Indian Ocean, which, when superimposed on the Indonesian Throughflow, produces a total transport of about 16 Sv flowing southward through the Mozambique Channel. Finally, the Antarctic Circumpolar Current (ACC) has a mean transport of 124 Sv, which south of Australia is enhanced by the 11 Sv going around that continent. The recirculation of the Indonesian Throughflow was identified previously by *Macdonald and Wunsch [1996]* and is also consistent with the *Ganachaud and Wunsch [2000]* results from later data ($16 \pm 5\text{Sv}$). The present estimated amplitude of the Indonesian Throughflow

Figure 3. (opposite) (top) Mean sea surface height changes estimated from a least-squares fit procedure over the 8 year period 1993 through 2000. Contour interval is 5 cm. domain. (middle). Estimated steric sea level change over the 8 year period 1993 through 2000 estimated from the model potential density field. Contour interval is 5 cm. (bottom) Least-squares fitted changes in sea level as observed by TOPEX/Poseidon over the same period, 1993 through 2000.

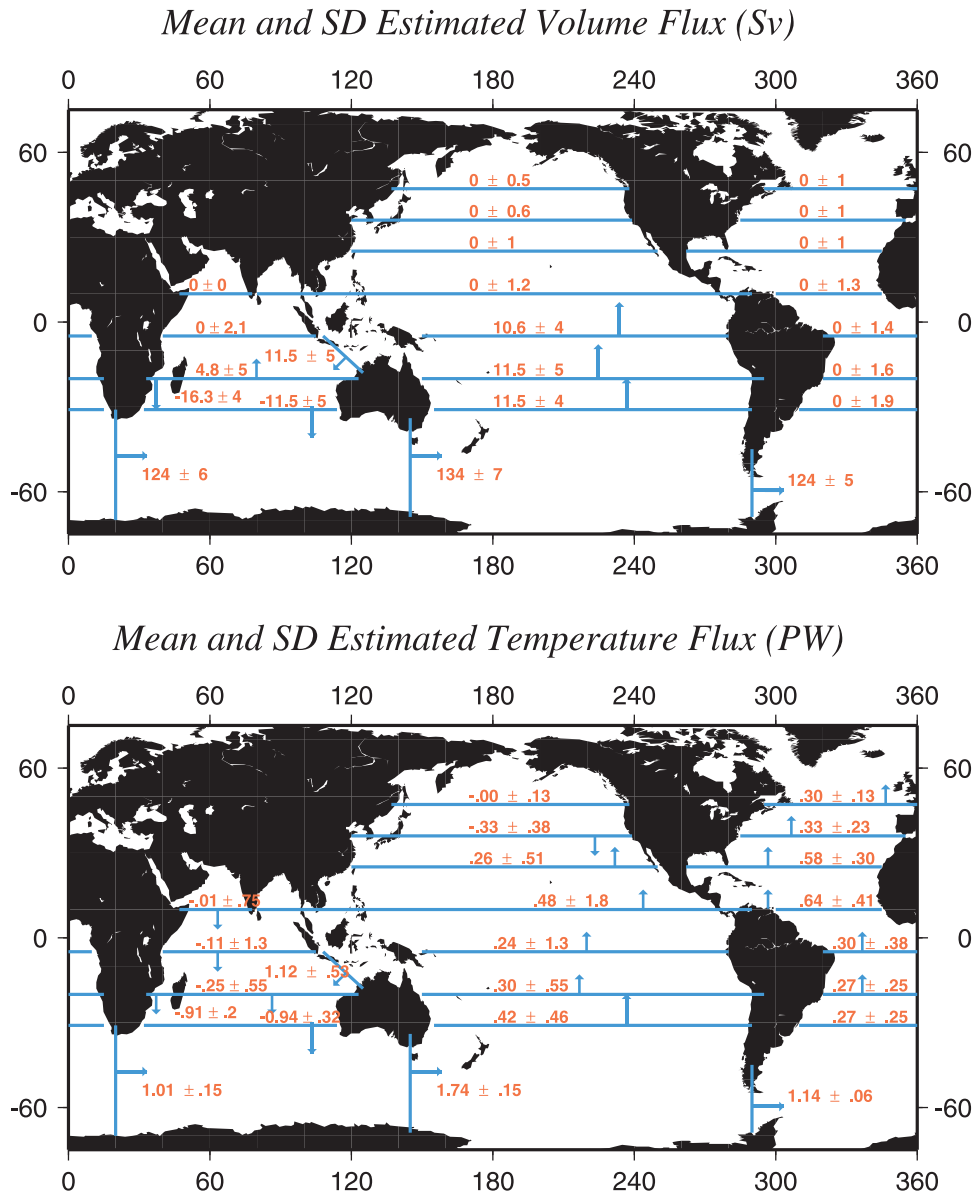


Figure 4. (top) Mean and standard deviations of volume flux (Sv) across sections as shown. (bottom) Mean and standard deviations of temperature transports (converted to Petawatts, PW) across various sections.

is in good agreement with independent results based on in situ data [Gordon, 1986; Roemmich *et al.*, 1996; Godfrey, 1996]. Various previous estimates exist also for the ACC transport. For example, Whitworth [1983] using a combination of moorings and hydrographic surveys, calculated a range of 118–146 Sv, with a mean of 121 Sv through the Drake Passage, but subject to various sampling errors. Nowlin and Klinck [1986] report 135 ± 5 Sv. Our estimated transport of 124 Sv lies between these estimates, but is lower, at one-standard error, than the 140 ± 7 Sv obtained by Ganachaud and Wunsch [2000].

4.2. Mean Heat Transports

[22] The heat content of volume V is given by

$$Q = \rho c_p \int \int \int_V \theta dz dx dy, \quad (2)$$

where c_p is the specific heat capacity, and ρ the water density. The time rate of change of Q is then,

$$\frac{\partial Q}{\partial t} = -\nabla \cdot \mathbf{F}_Q + H_Q, \quad (3)$$

where H_Q is the surface net surface heat flux and the zonally integrated meridional temperature transport (relative to a reference temperature of 0°) is

$$F_Q = \rho c_p \int_0^L \int_{-H}^0 v \theta dz dx. \quad (4)$$

Throughout this paper, we will refer to “temperature transport” where the mass balance is not closed, and

therefore integrals such as (4) depend on the chosen temperature scale. If the mass balance is closed, we will use the term “heat transport” (see *Bohren and Albrecht* [1998] or *Warren* [1999] for a discussion of the meaning of “heat transport”, which we will nonetheless continue to use as a shorthand for “energy transport”).

[23] Time mean values of F_Q in the model across various WOCE sections and their standard deviation are shown in Figure 4b. In the present solution, there is an average Indonesian Throughflow temperature transport of about 1.1 PW from the Pacific into the Indian Ocean. Most of this heat then moves southward through the Mozambique Channel. In contrast to the volume transport, the entire Indian Ocean shows southward temperature transport at the latitude of Mozambique. Some of it is communicated to the atmosphere between 20° S and 32° S and about 1 PW is released in the ACC region. Note that in our estimate, the 0.14 PW transported from the Indo-Pacific system into the Atlantic follows the “cold-water route” through the Drake Passage [see *Gordon*, 1986; *Rintoul*, 1991; *Macdonald*, 1998; *Ganachaud and Wunsch*, 2000]. This complete dominance by the cold-water route may be a consequence of the absence of any eddy variability or Agulhas ring formation in the coarse-resolution model.

[24] Figure 5 shows zonally integrated meridional heat transport globally and separately for the Atlantic and Pacific-Indian Oceans. Also shown are the zonal integrals obtained by *Ganachaud and Wunsch* [2000] from their box inversion. Although our estimates agree with theirs in the southern hemisphere and in the North Pacific, large discrepancies exist over the Atlantic where we estimate only about 50% of their amplitude, except at 10° N and at the southern end of the picture. However, this result is unsurprising in a 2° lateral resolution model in which the boundary currents are sluggish and diffuse, with the data unable to impose a different, sharper, spatial structure (accurate temperature, and hence heat transport, depends upon having correct values of the products of v and θ ; the high speed, high temperature Gulf Stream jet must then be properly rendered). Despite this resolution problem, the gross pattern of North Atlantic poleward heat transport is reproduced and its dependence on the closed nature of the poleward model boundaries or other model parameters has to be investigated. *Robbins and Toole* [1997] estimated 0.89 PW flowing southward across 33° S in the Indian Ocean which agrees well with our estimate of 0.94 PW. *Holfort and Siedler* [2001] estimated a net northward transport of 0.4 ± 0.25 PW in the South Atlantic across 30° S. *Wijffels et al.* [2001] obtain a net southward transport of the global

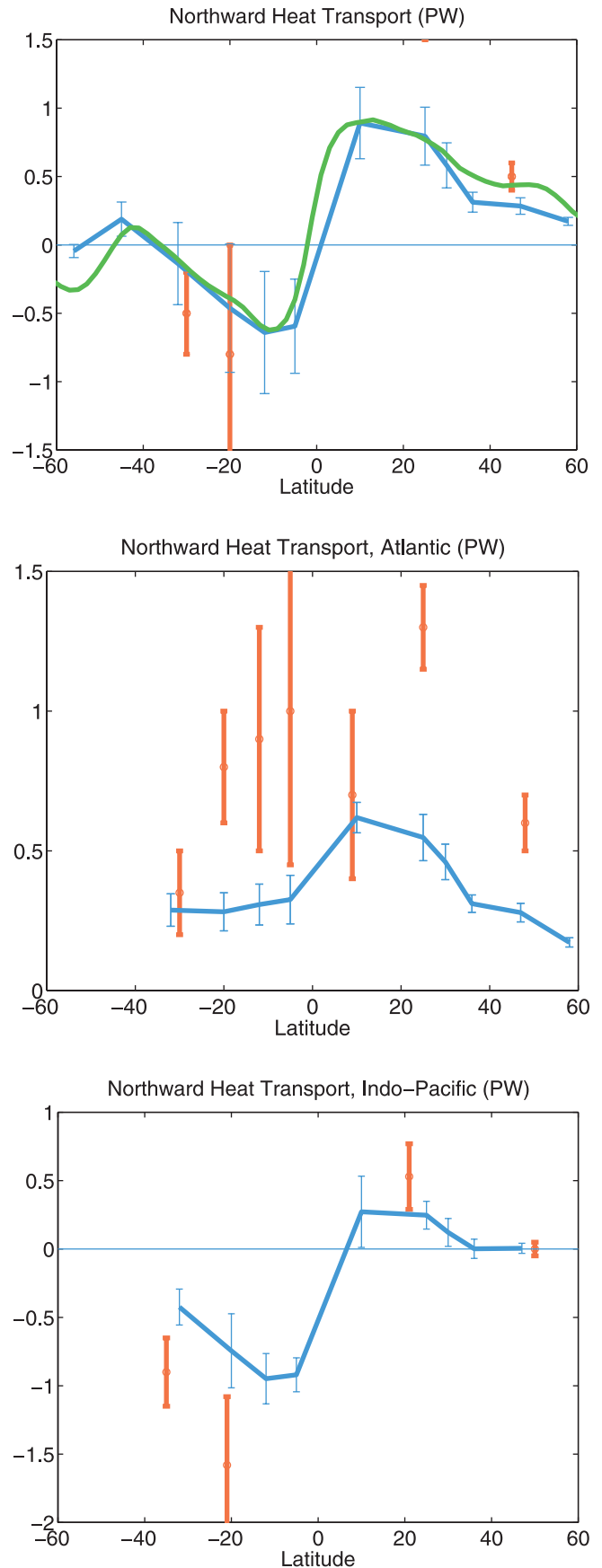


Figure 5. (opposite) Top panel: Integrated time-mean meridional heat transports for the global ocean estimated for various zonal sections in the model (blue curve). The blue bars are the STD of individual annual mean estimates. The green curve represents the ocean heat transport inferred from estimated surface heat fluxes. Middle and bottom panels: Estimated meridional heat transport across zonal sections in the model, evaluated separately for the Atlantic, Pacific–Indian Oceans. All red symbols represent estimates from *Ganachaud and Wunsch* [2000] and their formal uncertainties.

ocean of -0.46 ± 0.36 PW across 30°S and comparable to our -0.25 PW.

4.3. Mean Freshwater Transports

[25] In Figure 6 we show the zonally integrated meridional freshwater transports and their standard deviation, estimated as

$$F_W = \int \int_{-H}^0 \rho v (1 - S/S_0) dz dx. \quad (5)$$

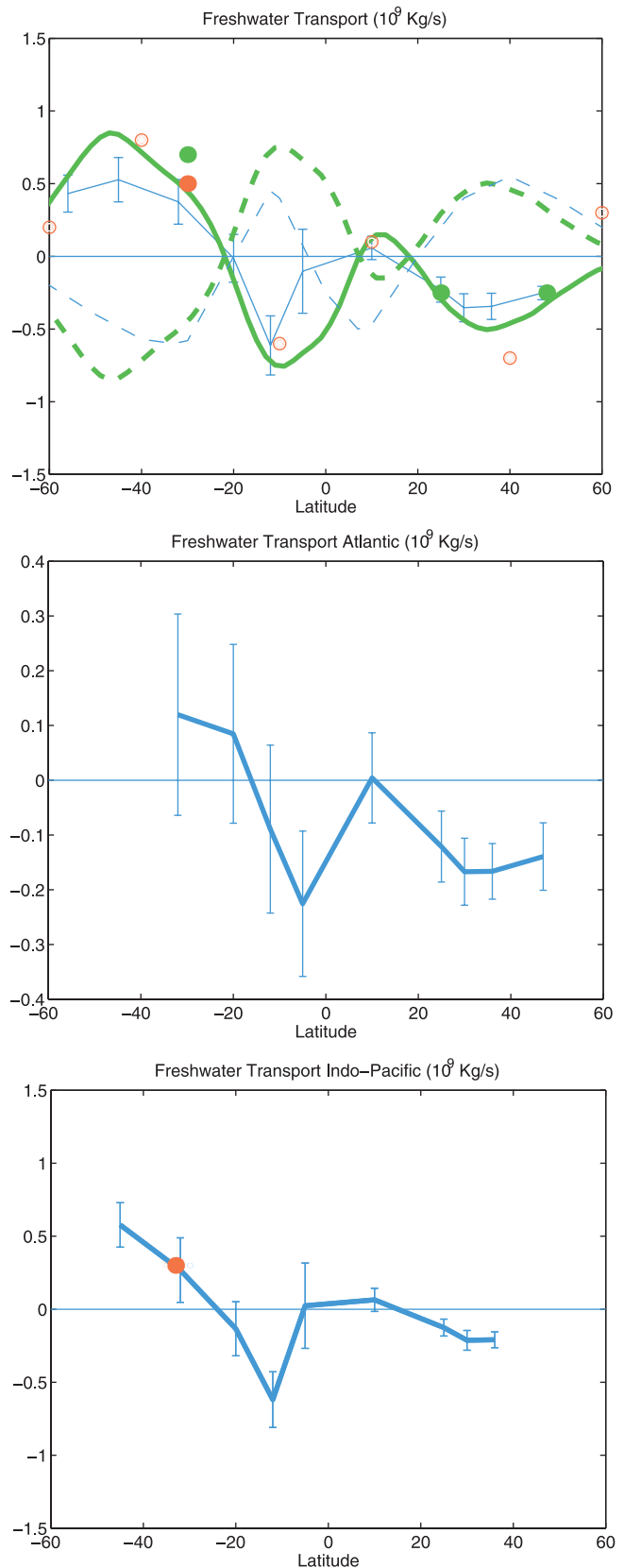
Freshwater transport estimates are in turn very similar to *Wijffels et al.* [1992] and *Macdonald and Wunsch* [1996] over most parts of the ocean, and with *Wijffels et al.* [2001] in the southern hemisphere. Global average transports are southward, north of 20°S , except around 10°N where they approach zero. Transports are of opposite sign further south. The resulting divergence in the ocean at 20°S must be balanced through atmospheric moisture transport. Further discussion follows below. The Pacific-Indian basin, if analyzed separately, transports freshwater across the equator from the southern into the northern hemisphere, consistent with *Wijffels et al.* [2001].

4.4. Basin-Integrated Mean Surface Fluxes

[26] Basin-integrated net surface heat and freshwater fluxes, corresponding to the divergences of the meridional transports in Figure 5 and Figure 6, are shown in Figure 7 as evaluated from the estimated surface net heat and freshwater flux fields (see also Stammer et al., submitted manuscript, 2002b). Global integrals and those for individual basins are both shown. The surface heat flux in the northern hemisphere outside the tropics is negative, that is, the ocean loses heat to the atmosphere. A similar result appears in the southern hemisphere between 10° and 40°S . The Southern Ocean, however, shows a pronounced warming pattern with net amplitude close to $1/3$ of that of the tropical ocean. This warming is mostly located over the Atlantic and Indian sectors of the ACC, again consistent with the *Ganachaud and Wunsch* [2000, their Figure 1] results. Heat is lost by the ocean over the South Pacific and Indian Oceans, while the Atlantic shows a net heat gain in the southern hemisphere. Note the small heat gain in the tropical Indian Ocean—indicating that most of the heat lost south of 10°S over that basin must be imported from the Pacific through the Indonesian Throughflow or the Southern Ocean.

Figure 6. (opposite) Top panel: Integrated time-mean meridional fresh water transports (in 10^9 kg/s) for the global ocean estimated from zonal sections in the model (blue curve). The blue bars are the STD of individual annual mean estimates. Green curve represents the ocean fresh water transport inferred from estimated surface freshwater fluxes. Green dotted line is an estimate of atmospheric moisture flux obtained as the negative of the green line. The blue dashed line is an estimate inferred by *Peixoto and Oort* [1983]. Middle and bottom panels: Estimated meridional fresh water transport across zonal section in the model, evaluated separately for the Atlantic, Pacific-Indian Oceans. The red open circles represent estimates from *Wijffels et al.* [1992]. Solid red and green dots are results from *Wijffels et al.* [2001] and *Macdonald and Wunsch* [1996], respectively.

[27] For freshwater, we find a net gain (excess precipitation) over the tropics, but also at high latitudes, especially over the ACC. Losses are quite similar in pattern between Atlantic, Pacific and Indian Ocean, although the Indian



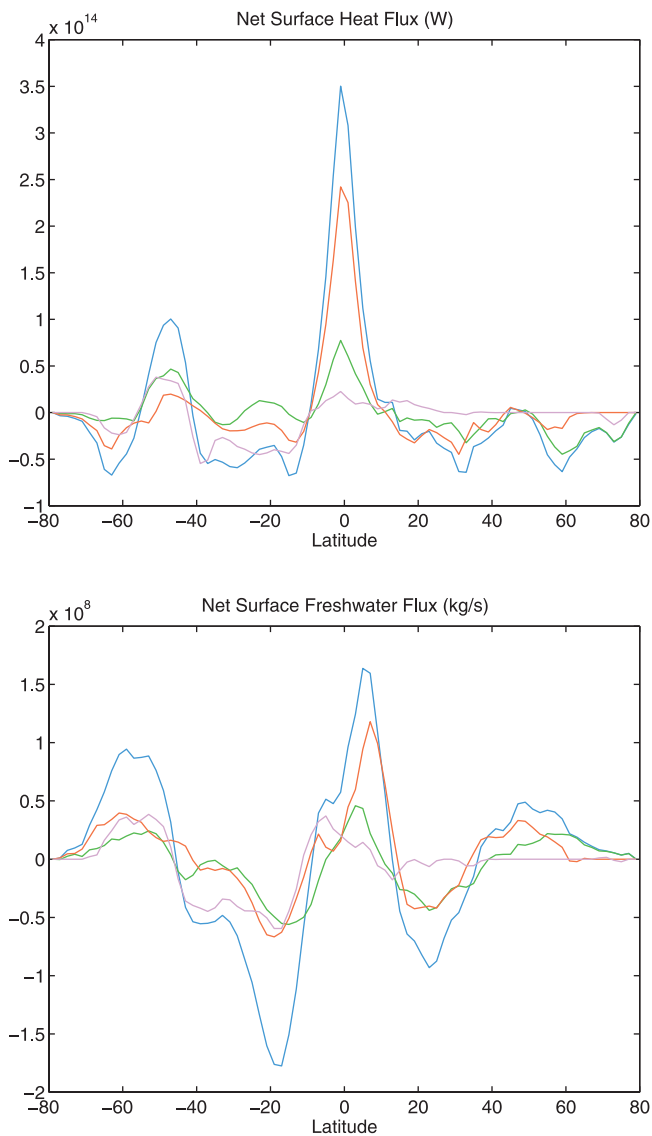


Figure 7. Zonally integrated heat (top in W) and surface fresh water fluxes (bottom in Kg/s), evaluated globally (blue curves) and over the Atlantic (green), Pacific (red) and Indian Ocean (magenta) sectors, respectively. Fluxes into the ocean are positive in both cases.

Ocean shows enhanced evaporation around 40°S. The salinity maximum in the North Atlantic and its origin in the strong freshwater loss over the eastern subtropical Atlantic, is well known. Here a similar forcing effect also appears in each of the other subtropical gyres.

[28] Integrating the net surface fluxes shown in Figure 7 meridionally from north to south provides an independent estimate of the time-mean horizontal heat and freshwater transports in the ocean. For a steady state system, they must be identical to transport estimates in the ocean. As can be seen from Figures 5 and 6, the estimates are similar, but not the same, illustrating again the fact that our model is not in equilibrium, and it is not obvious that it should be so.

[29] Previous studies by *Peixoto and Oort* [1983] and *Wiffels et al.* [2001] indicate a significantly enhanced excess of evaporation over the Indian Ocean resulting in a

0.35 Sv northward freshwater transport in the Indian Ocean and a 0.5 Sv northward freshwater transport globally. The resulting divergence here and over other parts of the global ocean must be balanced by atmospheric moisture transport. Respective atmospheric moisture transports, as inferred from our estimate, are added in Figure 6a. They are similar, but not identical to previous estimates based on *Peixoto and Oort* [1983] [see also *Wiffels et al.*, 1992]. More refined results from future estimations potentially can help improving our understanding of atmospheric moisture transports.

4.5. Volume and Heat Transports by Depth Range

[30] Figure 8 displays the time-mean volume and heat transports analogous to those in Figure 4b, but now separated by depth and temperature classes. The shallow nature of the Ekman cells is apparent—with high volume being transported in one direction near the surface and returned in the next depth class. As a consequence of this shallow character, their effects tend to be averaged out in the temperature classes. Water warmer than 4°C moves northward in the Atlantic and colder water returns southward. Near the equator and north of it, water warmer than 10°C carries the entire northward volume transport.

[31] Associated with the shallow overturning cell is a strong temperature transport, especially in the tropical oceans and over large regions of the Pacific Ocean. Note that most of the temperature transport variability occurs at temperatures above 10°C and that the temperature transports in the two lower temperature classes nearly compensate for each other. In general terms, the Indian Ocean carries warm water southward, and that is subsequently returned northward in the Atlantic via the coldwater route of the Drake Passage.

[32] In the South Pacific, a northward flow has contributions from all temperature classes, but with the main component lying above 4°C. This water is returned southward in the Indian Ocean—generally above 10°C. In the North Pacific, each temperature class seems to be balanced in terms of its own volume transport, and no large-scale net temperature transport, nor impact on the global budgets, is apparent.

5. Time-Varying Volume Transports

[33] While time-mean volume transports into enclosed basins are zero, their variability is not, indicating high-frequency storage effects over the larger basins. Standard deviations of volume transports at about 25°N are slightly larger than 1 Sv in the North Pacific and North Atlantic (see Figure 4) and are associated with a 0.5 cm high-frequency fluctuation of sea level on basin scale. Because the model has a free surface, in principle those fluctuations can represent the true local changes of volume in the ocean at high frequency. Transport variations occurring at very high frequencies (shorter than 30 days) are dominated by the rapid wind-induced Ekman transport and an associated barotropic return flow [see also *Fukumori et al.*, 1998; *Stammer et al.*, 2000; *Tierney et al.*, 2000; *Jayne and Marotzke*, 2001]. This and other variability is strongly constrained by the relatively dense altimetric data sets. Nonetheless, as we have seen already, both the altimeter data and the model results show large-scale regional sea level shifts indicative of long term accumulating effects.

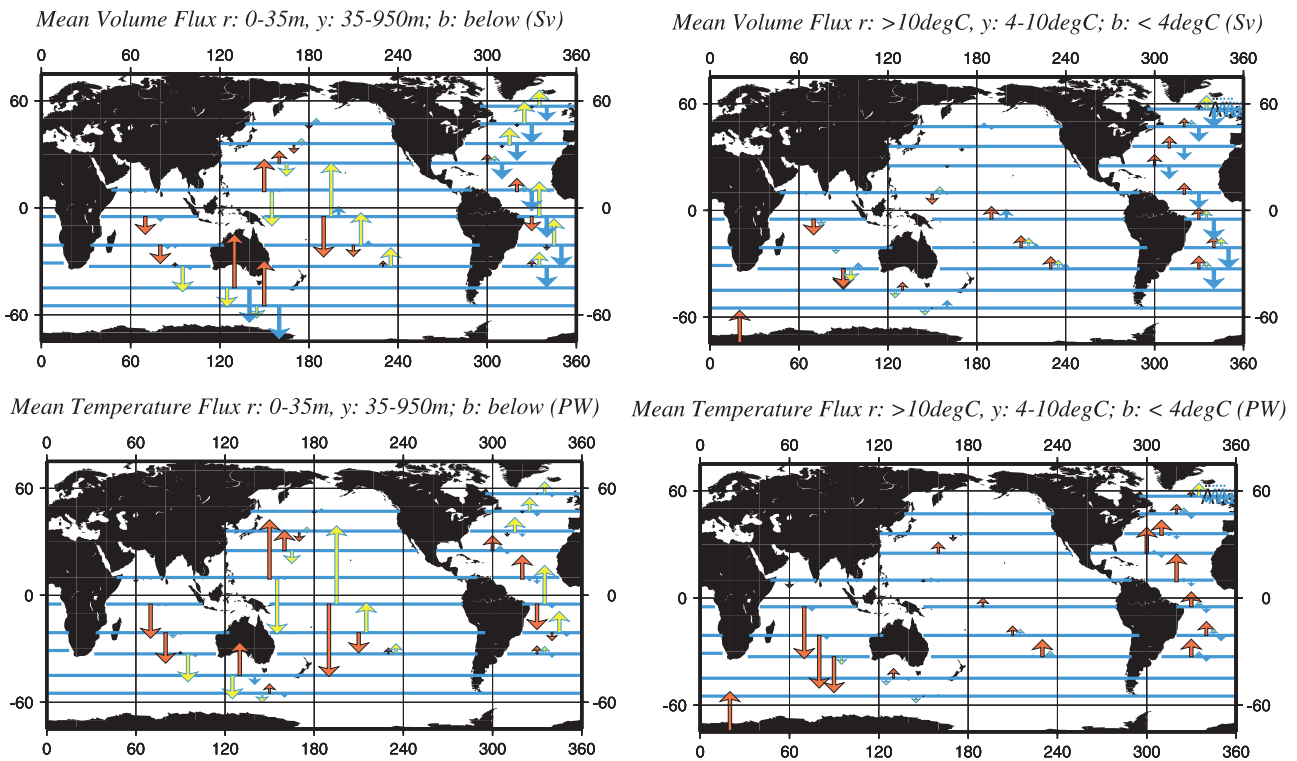


Figure 8. Maps of the mean volume (top) and temperature (bottom) transports. The left column shows results for depth classes, while the right column shows similar results for temperature classes. Reference vectors in the lower left part of the right panels show 20 Sv and 1 PW, respectively.

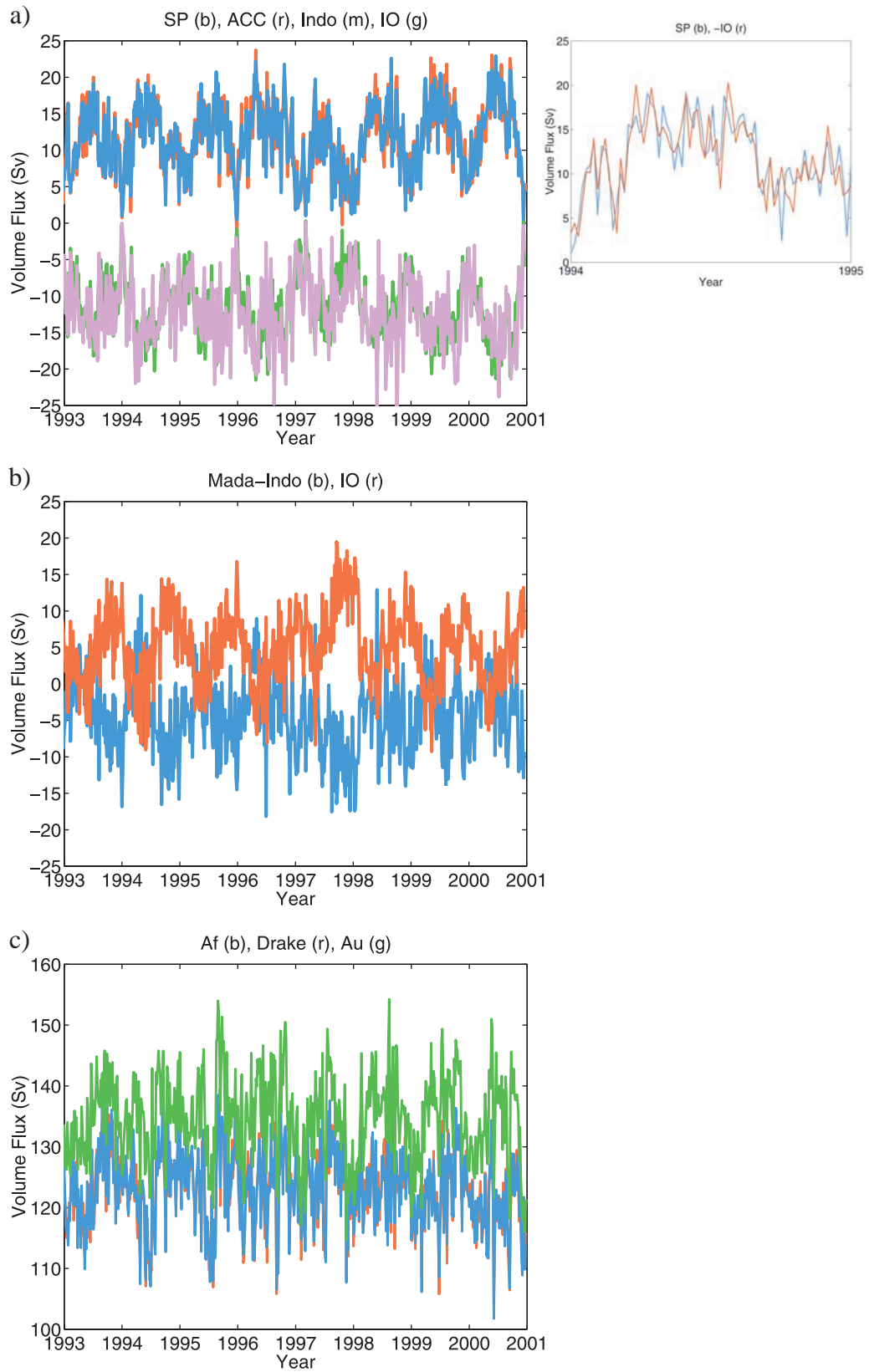
[34] Figure 9 shows time series of volume transport across 32°S in the South Pacific, and along the ACC south of Australia (with the ACC component through Drake Passage removed to demonstrate the local variability); also shown, with negative amplitude, are the flows through the Indonesian Throughflow, and the Indian Ocean across 32°S . A seasonal cycle superimposed on the high-frequency fluctuations is apparent, as is the striking degree to which the time series track each other on all timescales. The coincidence of the high-frequency variations across the Indo-Pacific basin is obvious from the inset, which shows only a one-year period of volume transports from the South Pacific and the southern Indian Ocean across 32°S . No phase lag between them is visible. Figure 9 also displays the time series in the Mozambique Channel Throughflow minus that from the Indonesian Throughflow; the difference compares well with the compensating transport moving northward across the remaining Indian Ocean at 20°S . Note also that the Indian Ocean shows almost no net northward volume transport during boreal winter, and a maximum of around 10 Sv between October and December.

[35] Apparently, there is a circulation system around Madagascar involving both the mean and the time-depend-

ent circulations alike, and that affects, in separate loops, the Indian Ocean and the entire Indo-Pacific system [Godfrey, 1996]. High frequency fluctuations of about 10–15 Sv in the Mozambique Channel have a standard deviation of about 5 Sv. The ACC south of Africa, and through Drake Passage, shows a strong seasonal cycle superimposed on high-frequency fluctuations. Near Australia, the additional, largely high-frequency, variability seen in the Mozambique Channel characterizing the Indo-Pacific closed loop circulation, is superimposed on the annual ACC transport variability.

[36] The above time series show that reports of “mean” volume transports from field programs of duration of a year or shorter cannot and should not be interpreted as representing the long-term average. In particular, the Indonesian Throughflow, the Madagascar Channel and Drake Passage transports would require many years of averaging to produce an accurate mean (and the model underestimates the high frequency variability owing to the absence of eddies and related motions). Moreover, a close inspection of Figure 9 reveals again a long-term drift in the model: the South-Pacific/Indian Ocean system is spinning up by about 1.5 Sv from 1993 through 2000. During the same interval,

Figure 9. (opposite) Top panel: Time series of volume transports from the South Pacific across 36°S (blue); along the ACC south of Australia (red) with the ACC component through Drake Passage removed. Negative values are from the Indonesian Throughflow (green curve) and the Indian Ocean across 36°S (magenta). Right inset shows a short segment of the time series in the Pacific Ocean (blue) and across the Madagascar Channel (red, plotted with opposite sign), to highlight the agreement on short periods. Middle panel: Time series of the Mozambique Channel Throughflow minus that through the Indonesian Throughflow (red curve) and the transport going north across the remaining Indian Ocean at 20°S (blue curve). Bottom panel: The ACC transports south of Africa, Australia, and through Drake Passage shown as blue, green and red curves, respectively.



the ACC system weakens by 2.5 Sv. Both changes represent roughly 10% of the eight-year averages.

6. Kinematics of Heat Transport Variations

[37] Figure 10 shows time series of meridional heat transports through the Indonesian Throughflow area, the Mozambique Channel and across 12°S in the Indian Ocean. A seasonal cycle is visible in all of them. It is largest across 12°S (2PW); for the Indonesian Throughflow it is only 0.5 PW and in phase with the Indian Ocean. In contrast, the annual cycle of the Mozambique Channel heat transport is even smaller and three months out of phase with the other two time series [cf. *Vranes et al.*, 2002].

[38] A significant seasonal cycle in the heat transport exists also along the ACC south of the Cape of Good Hope, with vigorous short-period variations superimposed (middle panel of Figure 10). Across Drake Passage, the transports are much more stable and vary primarily on a small amplitude seasonal cycle. In contrast, south of Australia, no visible seasonal cycle appears, and temperature transport variations have much of the character of the high-frequency volume transports there (compare Figure 9).

[39] All heat transport time series show interannual variability as well. To highlight the latter for the ACC system, we show in the bottom panel of Figure 10 annual mean heat transport values across 20°E, 140°E, and through Drake Passage. The figure is consistent with an eastward-migrating anomaly that shows up first south of Africa in 1994 and passes through Drake Passage in 1997. Its apparent speed is 10–20 cm/s. This transient might reflect a feature associated with an initial model adjustment. *White and Peterson* [1996] report a warm SST anomaly associated with an “ACC wave”, reaching the tip of Africa in 1994. However, their inferred 10 cm/s phase speed is somewhat slower than the value inferred here, and one cannot necessarily identify a feature velocity with a wave phase velocity.

[40] We now discuss the structure of the time-varying meridional heat transports, using initially, examples from the Atlantic. Figure 11 splits the total heat transport across 47°N, 9°N and 33°S into various contributions originating from different parts of the water column. The left column of the figure shows temperature transport in various depth classes: (0–50 m; 50–800, and below 800 m),

$$H_q = \rho c_p \left(\int_0^L \int_{-50}^0 v \theta dz dx + \int_0^L \int_{-800}^{-50} v \theta dz dx + \int_0^L \int_{-h}^{-800} v \theta dz dx \right). \quad (6)$$

[41] A summary of the overall result is that the largest part of the variability is associated with the shallow near-

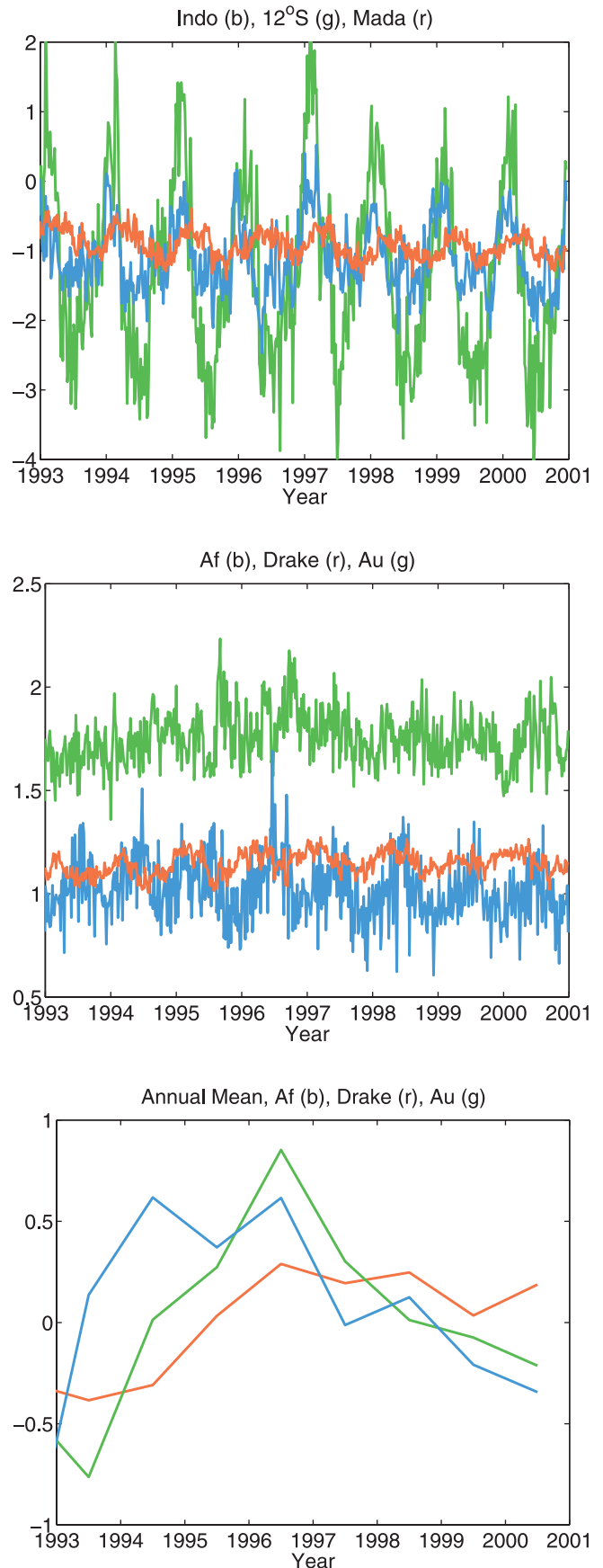


Figure 10. (opposite) (top) Timeseries of temperature transports through the Indonesian Throughflow (blue), across 12°S in the Indian Ocean, and through the Mozambique Channel (red). (middle) Timeseries of temperature transports across 20°E, 140° south of Australia and through Drake Passage (blue, green and red, respectively). (bottom) Same as in the middle panel, but plotted as annual mean transport anomalies.

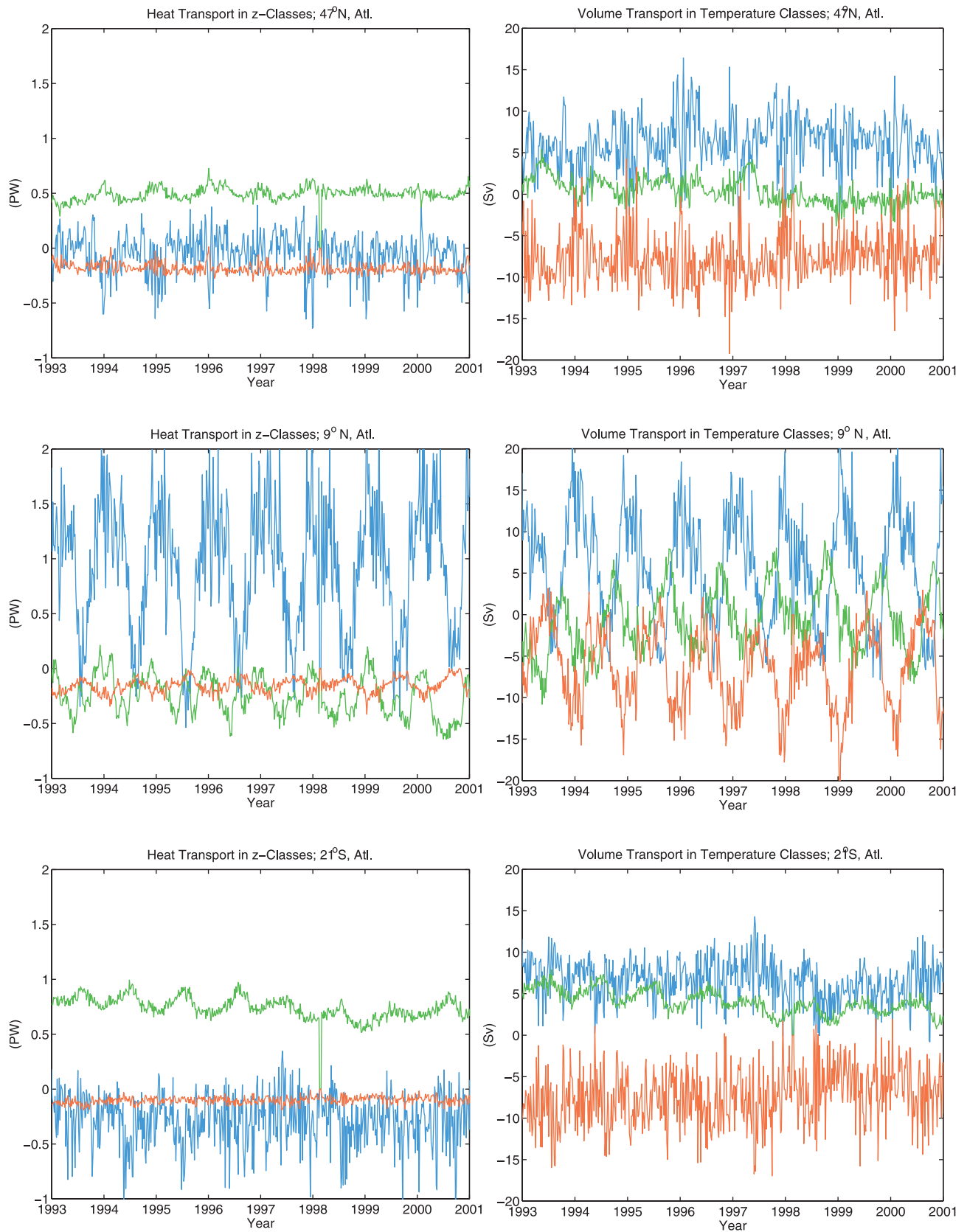


Figure 11. (left column) Timeseries of temperature transports across several latitude circles in the Atlantic as indicated in the panels. Transports were evaluated over the depth classes (0–50 m) (blue), (50–800 m) (green) and (800–bottom) (red). The right column shows time series of volume transport evaluated over temperature classes (>10°C) (blue), (10°C > θ > 4°C) (green) and (<4°C) (red).

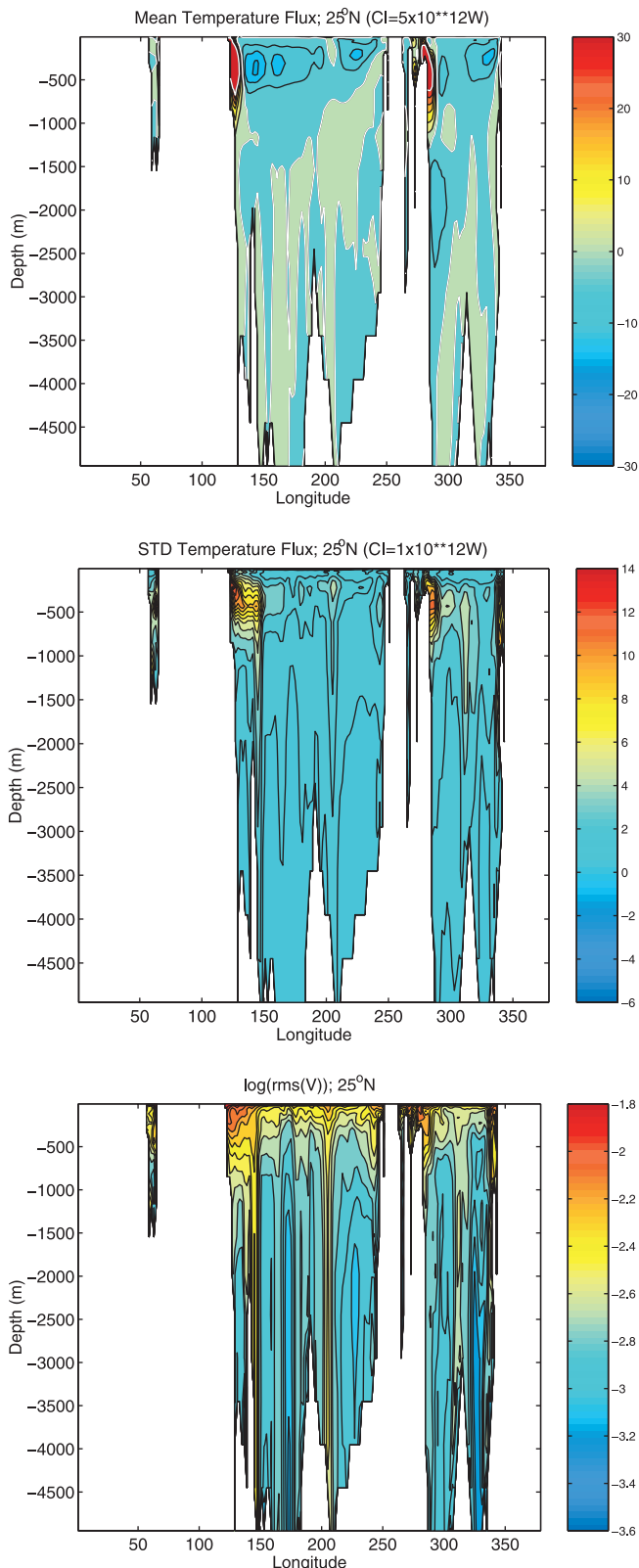


Figure 12. (top) Zonal sections of the time-mean \overline{vT} as a function of longitude and depth along 25°N . (middle) Standard deviation of vT which is almost the same as $v\overline{\theta}$. Enhanced variability of temperature transport that takes place in the top model level is not visible in this presentation. (bottom) Logarithm of the standard deviation of the meridional velocity component.

surface layers that are dominated by high frequency near-surface Ekman transports [cf. *Jayne and Marotzke, 2001*]. We note that the annual cycle increases toward the equator and that the high-frequency variations in temperature transports in the near-surface range are not compensated instantaneously by deeper compensating transports at most latitudes. Only at 47°N can significant compensation be seen during winter months. As a result, most of the corresponding heat is stored locally, and is then redistributed by the shallow layers. In contrast, the deeper layers show more seasonal to interannual variations. Nevertheless, the shallow wind-driven variations also display interannual variations of amplitudes similar to the deeper part, especially in high latitudes.

[42] Also shown in the figure are volume transports, but split into temperature classes: ($\theta > 10^\circ\text{C}$; $4^\circ\text{C} < \theta < 10^\circ\text{C}$; $\theta < 4^\circ\text{C}$) so that,

$$H_v = \left(\int_0^L \int_{z(10^\circ)}^0 v \theta dz dx + \int_0^L \int_{z(4^\circ)}^{z(10^\circ)} v \theta dz dx + \int_0^L \int_{-h}^{z(4^\circ)} v \theta dz dx \right). \quad (7)$$

It appears that the near-surface volume transport fluctuations with temperatures warmer than 10°C are largely compensated by the deep cold return flow at high frequencies. This result does not apply however, to the seasonal cycle. As an example, we can see an intriguing phase shift between the three curves at 9°N , suggesting that the deep southward flow is maximum before the northward surface flow. The intermediate temperature flows between 4° and 10°C seem decoupled and shifted in phase even further, showing a maximum northward flow a few months after the deep layers and a few months before the near-surface ones.

[43] Volume and heat transport are of course, not uniformly distributed along the sections in their time mean and variability component. Figure 12 displays zonal sections of the time-mean \overline{vT} as a function of longitude and depth along 25°N . Similar fields, but for the southern hemisphere along 21°S are displayed in Figure 13. Variations in the very first level are of the same order as the maximum changes around 500 m depth, but do not show up in the figure. Note the similar structures of temperature transports in the North Pacific and North Atlantic, but the lack of a negative (southward) transport at the deep western boundary in the Pacific Ocean. The standard deviation of vT is almost the same as that of $v\overline{\theta}$. Note the substantial fluctuations in middepth, especially near all western and eastern boundaries, but also over pronounced topographic features.

[44] Note also the second-mode structures of the temperature transports and their variances in almost all western and eastern boundary currents at this latitude. Highest variations in transports are generally located at the transition in the mean transports from positive to negative. Note also the large southward transports on both sides of Madagascar, which extends over a large fraction of the entire water column.

[45] To demonstrate that most of the heat transport variations below 500 m depth in Figures 12 and 13 are driven by changes in the flow field and not by temperature

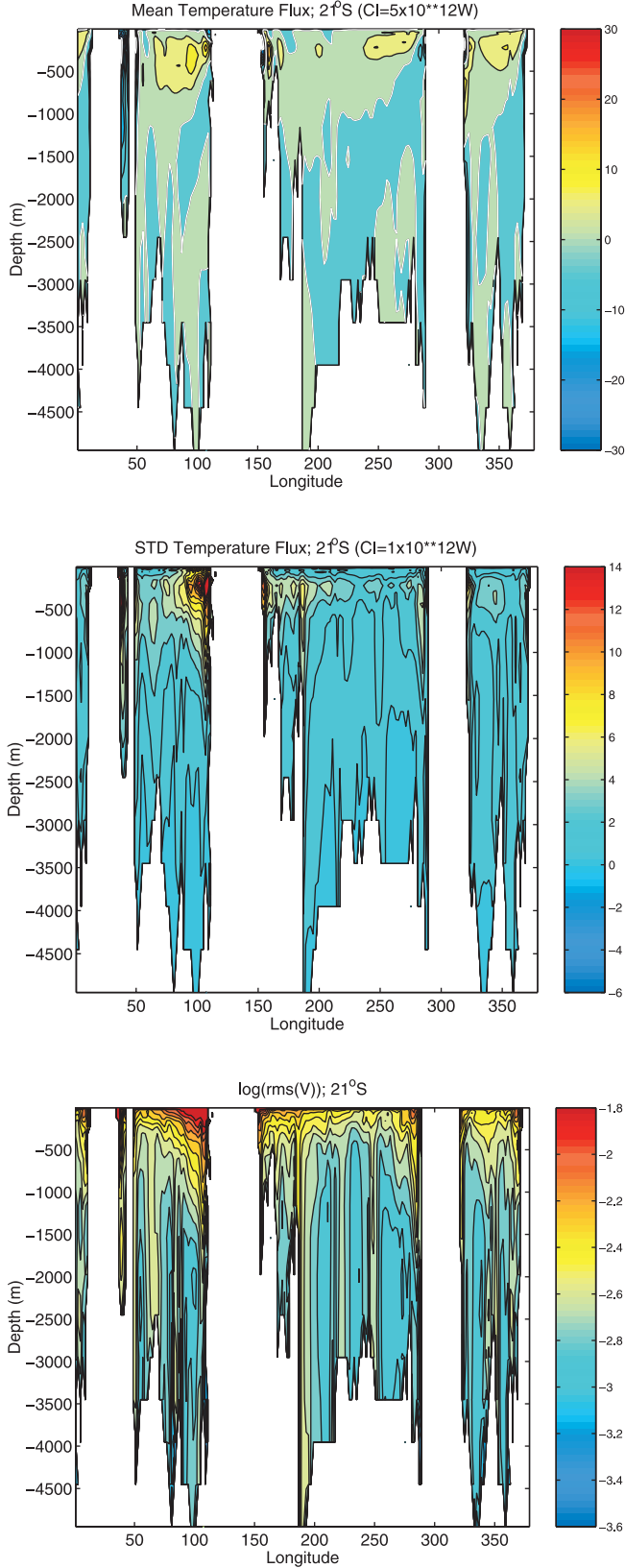


Figure 13. (top) Zonal sections of the time-mean \overline{vT} as a function of longitude and depth along 21°S . (middle) Standard deviation of vT which is almost the same as $v'\overline{\theta}$. (bottom) Logarithm of the standard deviation of the meridional velocity component.

fluctuations, we display in both figures the logarithm of the standard deviation of cross-section volume transport. High variability is associated primarily with shallow boundary currents on both sides of the Indian and Pacific Oceans. However, enhanced flow variability in the northward velocity component can also be seen along the flanks of all steep topographic features in the model. In the Southern Ocean, the Ninetyeast Ridge in the central Indian Ocean and the East-Pacific Rise were previously identified as a region of vigorous barotropic variability [e.g., Fukumori *et al.*, 1998; Stammer *et al.*, 2000]. Figures 12 and 13 indicate that enhanced variability is a universal characteristic near steep topography.

[46] Transports can be split into various components. To investigate which ones are most prominent, write the transport across each of the sections in the form,

$$H_q(t) = \int_0^L \int_{-H}^0 \overline{v\theta} dz dx + \int_0^L \int_{-H}^0 v'(t)\overline{\theta'} dz dx + \int_0^L \int_{-H}^0 \overline{v}\overline{\theta'} dz dx + \int_0^L \int_{-H}^0 \overline{v\theta'} dz dx, \quad (8)$$

where x -integrals are along zonal sections, and the bar indicates the time-average. This decomposition is shown in Figure 14 (omitting the first right-hand term). The last term, in $\overline{\theta'}$, gains importance toward high latitudes and is responsible for almost all seasonal changes there. Note that both terms involving v' tend to be of opposite sign at mid- and high latitudes during winter seasons (i.e. in winter time enhanced meridional flow carries colder water), and are in phase during summer. Toward low latitudes, most of the variability is in the $v'\overline{T}$ term, while the two other terms are very small. In summary, accurate flow estimates are the most important information for estimating the time-varying temperature transports in low latitudes, while at high latitudes both the changing flow and temperature fields must be known.

[47] Another way to look at the temperature/heat transports is to separate their contributions to the vertical overturning circulation from that of the horizontal gyre effect, or equivalently the vertical mean contribution from the vertically varying one. To do so, define $\tilde{V}(z, t)$ as the zonal average of $V(x, z, t)$, $\tilde{V}'(x, z, t) = V(x, z, t) - \tilde{V}(z, t)$ and V_d as the vertical average and $V_d'(x, z, t) = V(x, z, t) - V_d$. Then the heat transport can be written as [see also Böning and Bryan, 1996]

$$F_q = \rho c_p \int_0^L h(x) V_d T_d dx + \int_0^L \int_{-h(x)}^0 V_d' T_d' dz dx = F_0 + F_1, \quad (9)$$

i.e., split into a depth independent, and depth-dependent components. (Note that purely baroclinic flows produce nonzero vertical average volume transports, and it would be incorrect to call F_0 the “barotropic” component.) $h(x)$ is the water depth. Equivalently, we can write,

$$F_q = \rho c_p \left(\int_0^L \int_{-h(x)}^0 \tilde{V} \tilde{T} dz dx + \int_0^L \int_{-h(x)}^0 \tilde{V}' \tilde{T}' dz dx \right) = F_{OT} + F_G, \quad (10)$$

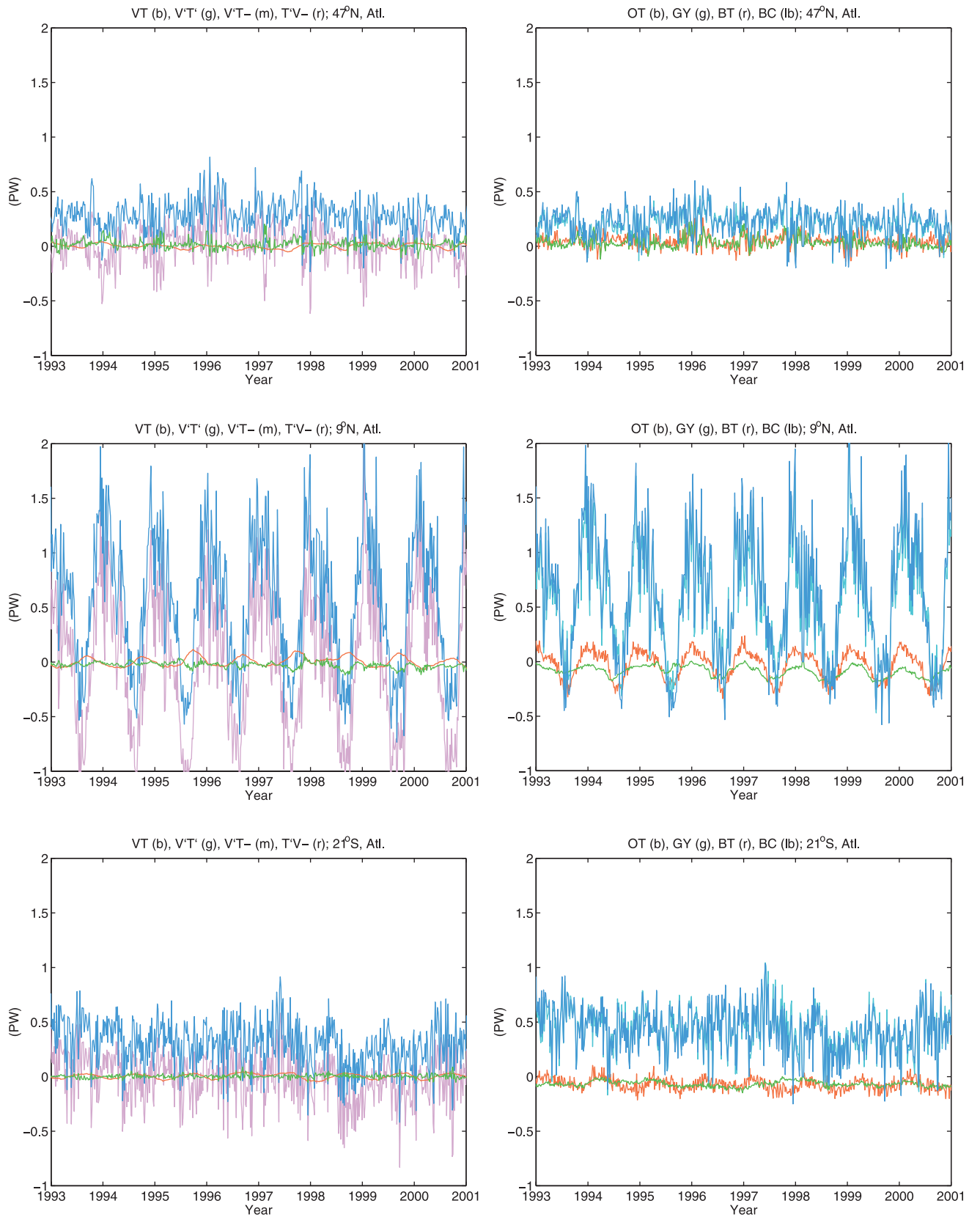


Figure 14. (left) Timeseries $H_O(t) = \int \int v \theta dz dx$ (blue curves) across zonal sections with locations given in the panels. Also shown are $\int \int v' \theta' dz dx$, $\int \int \bar{\theta}' dz dx$ and $\int \int \bar{v} \theta' dz dx$ as green, magenta and red lines, respectively. (right) Temperature transport time series evaluated as contributions from the overturning (OT; blue), the gyre (GY; green), the barotropic (BT, red) and baroclinic circulation (BC, light blue), respectively. See text for details.

i.e., divided into overturning and gyre components. Further subdecomposition is possible [e.g., *Jayne and Marotzke, 2001*] and these decompositions are not unique.

[48] Several surprising results are visible from the four F_j terms shown in Figure 14 as zonal integrals. High frequency changes in F_1 and F_{OT} are almost identical and dominate the variability. As discussed by *Jayne and Marotzke [2001]*, this variability arises from the variable Ekman transport and a true barotropic return flow. Although smaller in amplitude, F_0 and F_G are significant. Near the equator, F_0 and F_G show an interesting seasonal cycle. Further south, F_0 becomes more significant, with F_G becoming very small. Note the transport estimates near 33° S, which show the F_0 diverging from the F_G , as well as a clear separation of the other two estimates.

[49] Figure 15 shows time mean values of F_j as a function of latitude for the global ocean and separately for the Atlantic and Indo-Pacific sectors. Surprisingly, around 25° N, F_0 is the dominant transport mechanism on the global average. Toward higher latitudes, all F_j become small, but equatorward, F_1 and F_{OT} dominate. (The reader is reminded that these are not additive contributions.)

[50] In the Indo-Pacific F_0 is large in the northern hemisphere where it is largely compensated by F_1 . In contrast, south of the equator F_1 and F_{OT} dominate the southern Indian Ocean. In the Atlantic, F_1 or F_{OT} dominate, but around 25° N, F_0 is enhanced. A comparison with Figures 4.11 and 4.12 in the work of *Böning and Bryan [1996]* shows that our results are almost identical to theirs in terms of the general structure, especially for the overturning component of their $1/3^\circ$ CME results. But the present gyre component is somewhat smaller than their result from a 1° model version of the North Atlantic. In agreement with the present results, the CME shows an enhanced F_0 , although it is slightly further north, near 30° N. The basic difference is that we obtain only a small fraction of their depth-independent amplitude—with more than 1 PW carried in that form in the CME result. The global structure of temporal variability in the heat budget cannot be reduced to any single dominant mechanism.

7. Regional and Global Heat Balances

[51] An important question concerns the way in which the ocean transports and stores heat and how it communicates any regional heat transport divergences through the surface to the atmosphere. Variations in heat storage will contribute to the sea level changes discussed above. Consider the heat content changes in various regions of the Pacific Ocean as shown in Figure 16. Region 1 includes the Kuroshio Extension in the North Pacific. Zonal and meridional horizontal transport convergences as well as their net contribution to the temperatures fluxed into the region are displayed in the upper panel of Figure 17. The net lateral

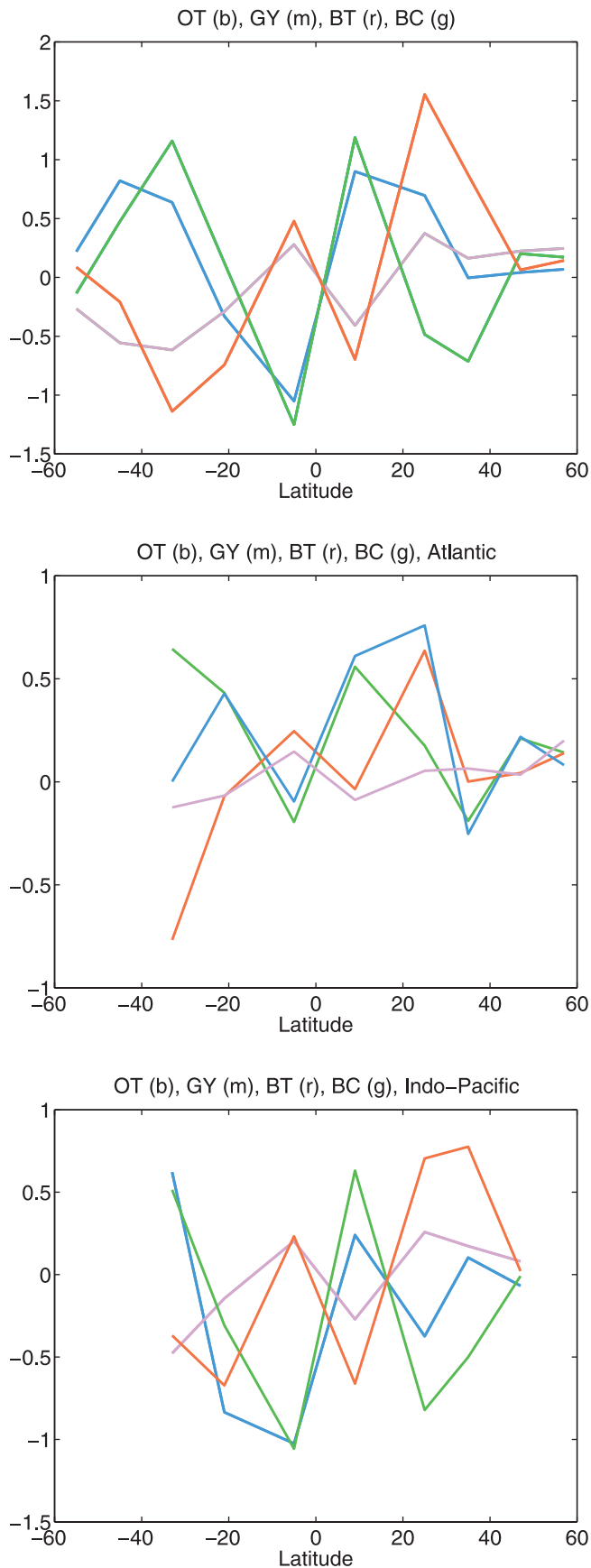


Figure 15. (opposite) (a) Time-mean of zonally integrated heat transports resulting from the overturning (OT; blue), the gyre (GY; magenta), the barotropic (BT, red) and baroclinic circulation (BC, green), respectively. The middle and bottom panels show similar results but separately for the Atlantic and Indian-Pacific sectors.

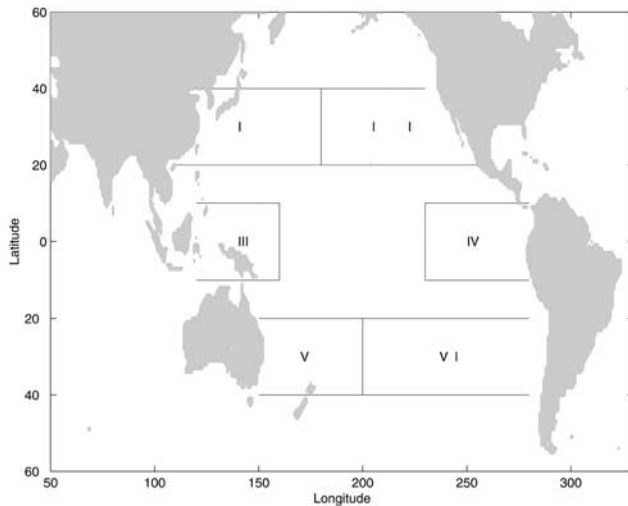


Figure 16. Map showing regions 1–6 for which the heat content budgets are shown in Figures 17–19.

influx is clearly positive, indicating that the region is being supplied by heat from the ocean.

[52] In the middle panel of the same column, we show again the net horizontal temperature transport convergences,

together with the net surface heat flux of the same region and the net oceanic heat content change dQ/dt . The net oceanic heat influx is balanced by a net surface heat flux over that region of -8.8 W/m^2 leading to a almost stable heat content that varies only on the seasonal cycle (bottom panel).

[53] Further to the east (Region II) the situation is somewhat different. Here the heat content is steadily rising over the six-year integration period. Convergence of the horizontal transports is positive zonally and negative meridionally. The net effect is close to zero over the first part of the period, but turns negative subsequently, i.e., the ocean then carries heat out of this region. Net surface heat transport is also positive (6.6 W/m^2) and the heat content increase here can now be identified as a joint effect of horizontal transport convergence and surface transport during the first few years. The negative transport convergence subsequently plus the anomalously large winter-time cooling during the last ENSO event halts the trend in the heat content increase during 1997 and 1998. This is a good example showing that, although small in amplitude, oceanic transports and convergences, accumulate over long periods to produce substantial effects.

[54] Regions III and IV are located at the western and eastern side of the tropical Pacific, respectively (Figure 18). Horizontal transport convergences are large here and show clear signs of ENSO effects, especially during 1997 when at

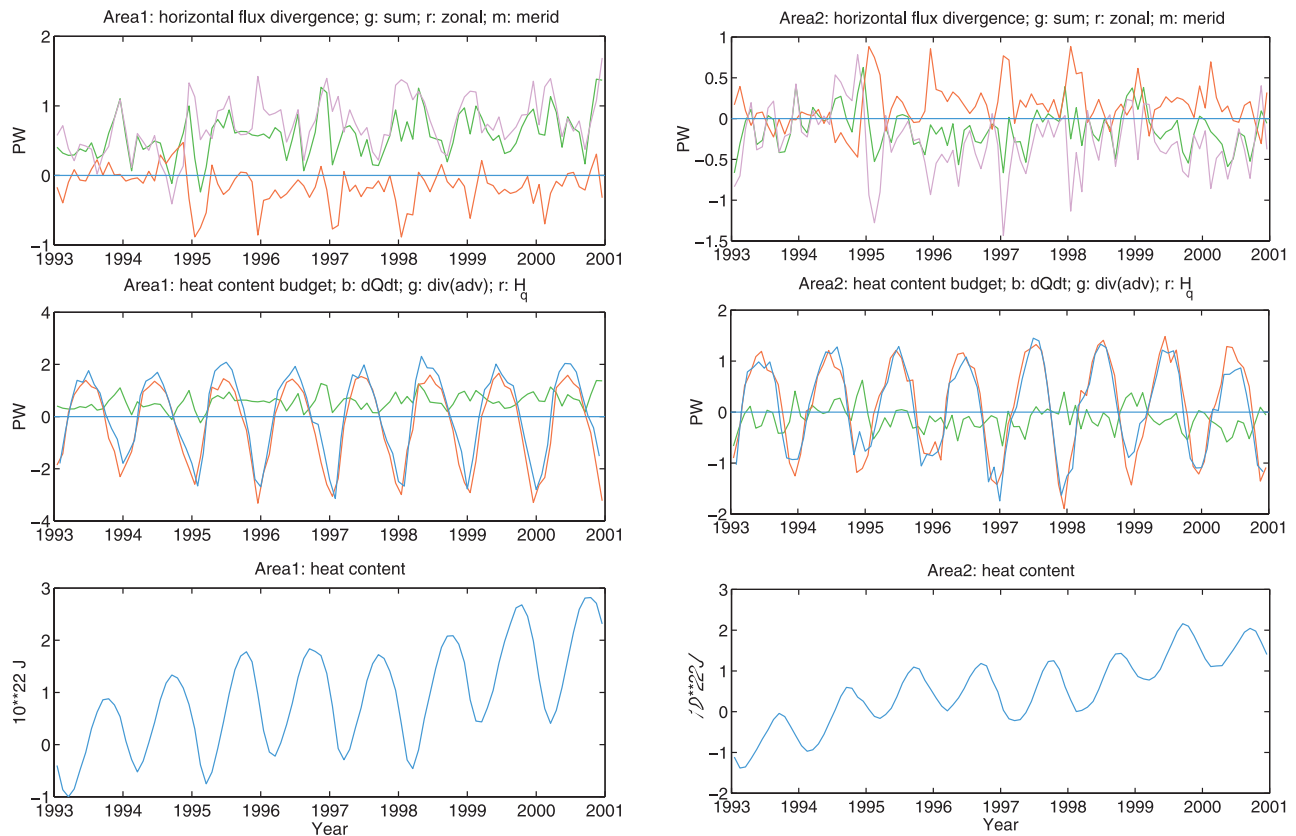


Figure 17. Horizontal temperature flux convergence in region 1 (left) and region 2 (right), plotted separately for the zonal contributions (red), the meridional contributions (magenta) and the net convergence (green). (middle) Horizontal temperature flux convergence (green), net surface heat flux (red) and time-rate of change of heat content in the region (blue). (bottom) Timeseries of heat content (blue).

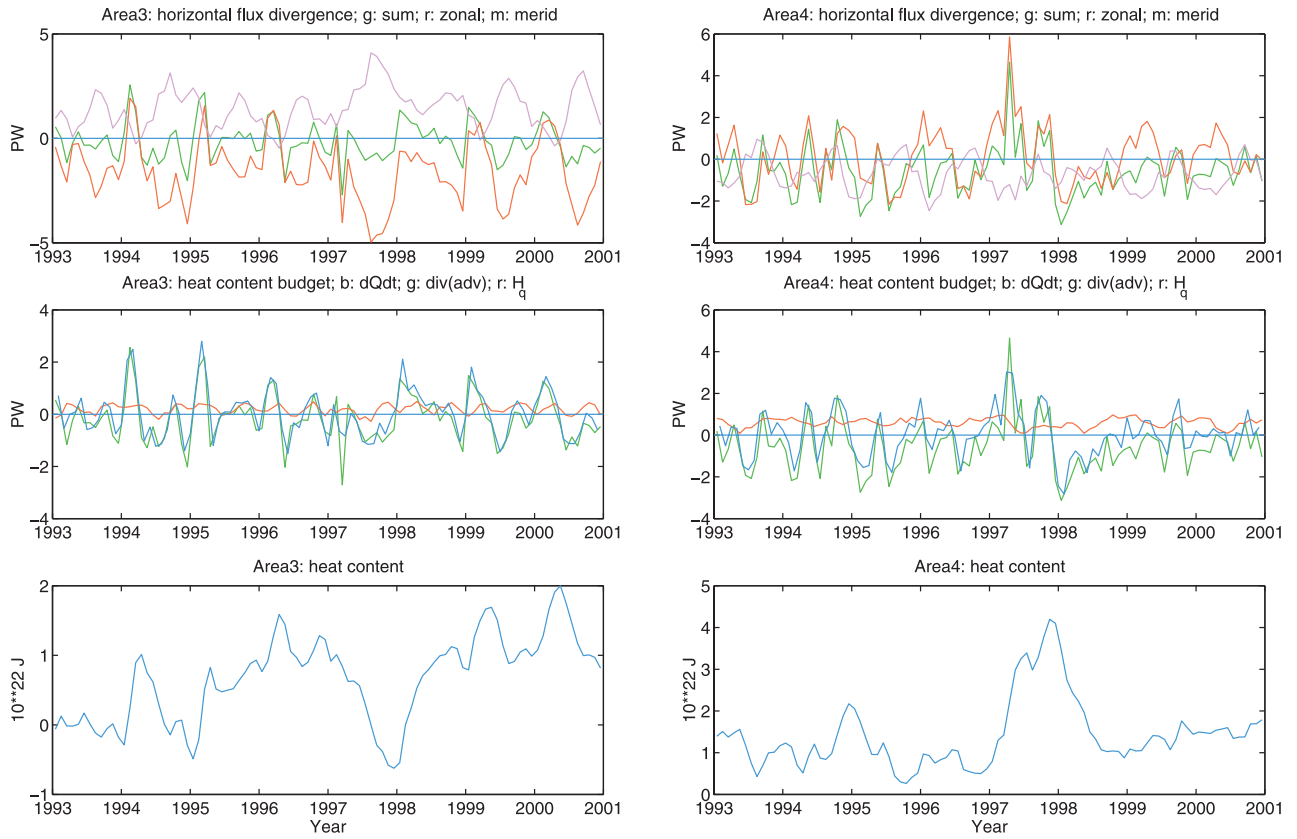


Figure 18. Same as in Figure 17, but for areas 3 and 4.

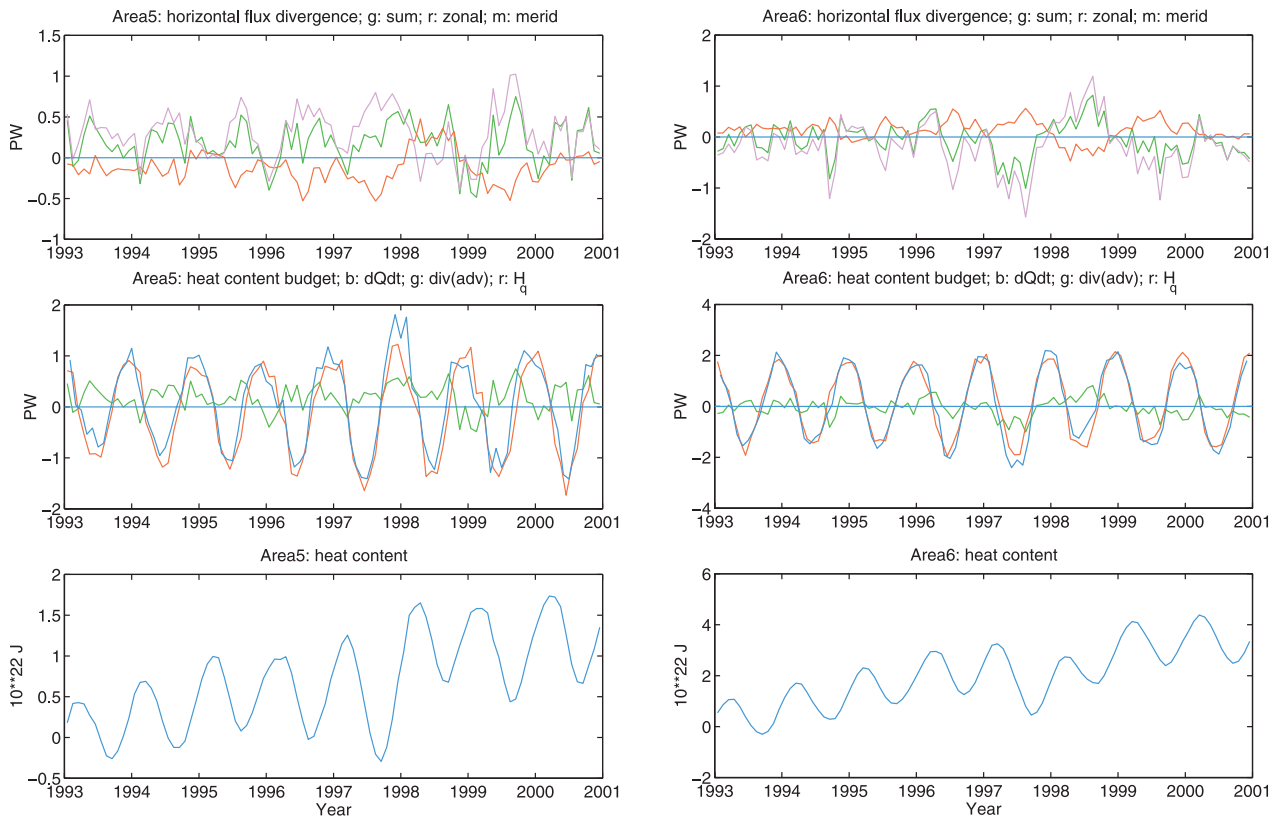


Figure 19. Same as in Figure 17, but for areas 5 and 6.

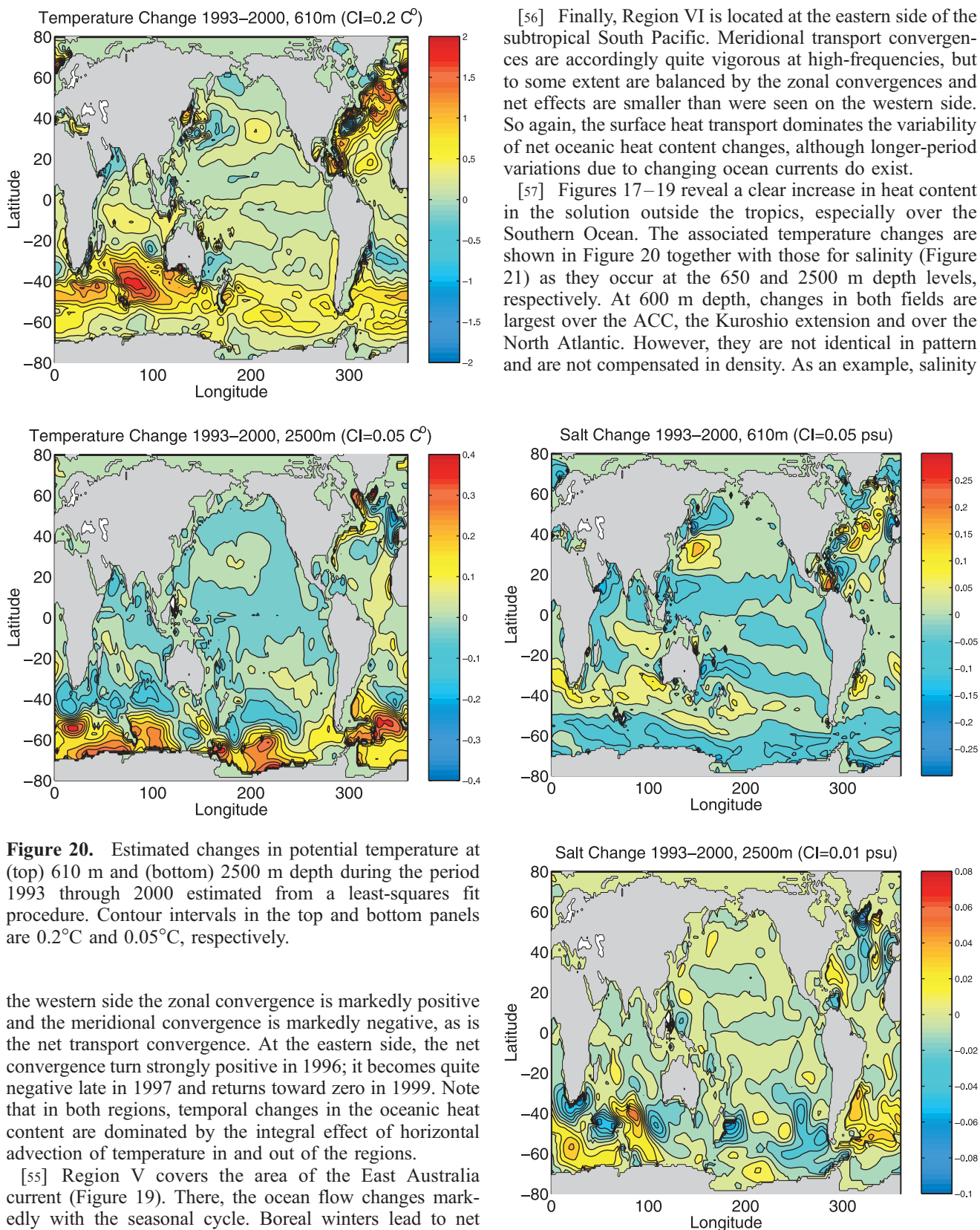


Figure 20. Estimated changes in potential temperature at (top) 610 m and (bottom) 2500 m depth during the period 1993 through 2000 estimated from a least-squares fit procedure. Contour intervals in the top and bottom panels are 0.2°C and 0.05°C, respectively.

the western side the zonal convergence is markedly positive and the meridional convergence is markedly negative, as is the net transport convergence. At the eastern side, the net convergence turn strongly positive in 1996; it becomes quite negative late in 1997 and returns toward zero in 1999. Note that in both regions, temporal changes in the oceanic heat content are dominated by the integral effect of horizontal advection of temperature in and out of the regions.

[55] Region V covers the area of the East Australia current (Figure 19). There, the ocean flow changes markedly with the seasonal cycle. Boreal winters lead to net inflow of temperature and the influx becomes slightly negative six months later. The changes in the oceans net heat contents are somewhat smaller than the net surface heat transport fields would suggest and heat content variations on seasonal and interannual timescale are strongly influenced by variations in horizontal transport convergences.

[56] Finally, Region VI is located at the eastern side of the subtropical South Pacific. Meridional transport convergences are accordingly quite vigorous at high-frequencies, but to some extent are balanced by the zonal convergences and net effects are smaller than were seen on the western side. So again, the surface heat transport dominates the variability of net oceanic heat content changes, although longer-period variations due to changing ocean currents do exist.

[57] Figures 17–19 reveal a clear increase in heat content in the solution outside the tropics, especially over the Southern Ocean. The associated temperature changes are shown in Figure 20 together with those for salinity (Figure 21) as they occur at the 650 and 2500 m depth levels, respectively. At 600 m depth, changes in both fields are largest over the ACC, the Kuroshio extension and over the North Atlantic. However, they are not identical in pattern and are not compensated in density. As an example, salinity

Figure 21. Estimated changes in salinity at (top) 610 m and (bottom) 2500 m depth during the period 1993 through 2000 estimated from a least-squares fit procedure. Contour intervals in the top and bottom panels are 0.05 and 0.01, respectively.

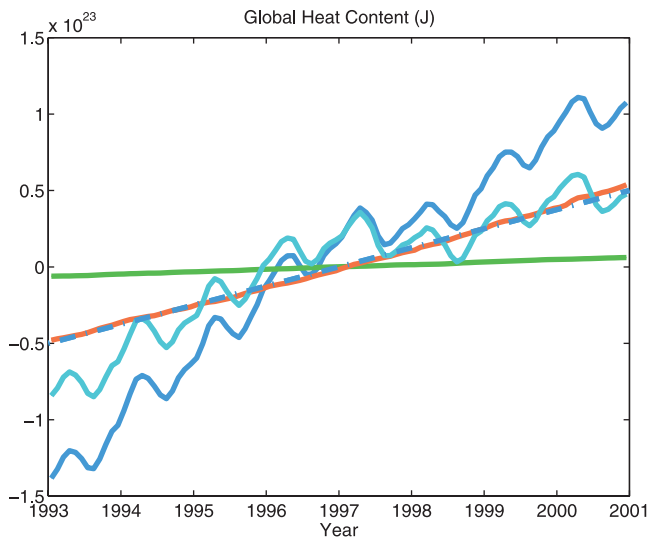


Figure 22. Global heat content (blue) and respective values evaluated separately over the top 510 m, from 510 to 2200 m and below (cyan, red and green curves, respectively). Also shown as blue dash-dotted line is an estimate of global heat content increase obtained from *Levitus et al.* [2001].

changes are large over the Kuroshio, while temperature seems to change more pronouncedly further east over the central Pacific as one would expect from a Pacific Decadal Oscillation (PDO) [cf. *Schneider et al.*, 2002].

[58] Deeper down in the water column, temperature and salinity drifts are almost negligible in some regions, such as the tropical Pacific, indicating that vertical numerical diffusion does not play a key role in the erosion of T/S structures. But temperature and salt changes are large near source regions of deep water masses. In the southern oceans those are the Ross and Weddell Seas. In the North Atlantic a clear path of anomalously warm water along the deep western boundary current is obvious, originating from the Labrador Sea and Irminger Sea and reaching down to the latitude of Florida.

[59] A comparison of the changes in SSH (Figure 3) with those in temperature and salinity reveals that over the Southern Ocean, the salt effects seems to be as important as temperature, and in some places dominates SSH changes. The same conclusion applies to the Kuroshio. In contrast e.g., in the central subtropical North Pacific, shallow temperature changes seem to dominate the SSH changes, while the Southern Ocean shows a clear relationship between deep temperature changes and SSH trends.

[60] Patterns of temperature changes similar to those shown in Figure 20 could underlie the global changes in temperature and heat content reported recently by *Levitus et al.* [2001] [see also *Barnett et al.*, 2001]. Our results indicate that warming in the deep ocean is far from uniform, geographically and could have relatively short advective timescales in regions connected to water mass source regions [see also *Döscher et al.*, 1994].

[61] For a comparison with the *Levitus et al.* [2001] results, we show in Figure 22 a time series of the global heat content of our solution together with those computed

separately over the top 510 m, from 510 to 2200 m, and from 2200 m to the bottom. A temporal mean was removed from all curves. The global increase in heat content is about 2×10^{22} J over the 8 year period 1993 through 2000, a number that is about twice the estimate provided by *Levitus et al.* [2001]. The total increase in heat content is consistent with the 4.7 W/m^2 positive imbalance in global surface heating of our solution; the discrepancy to *Levitus et al.* results could be explained by an excess of only 2 W/m^2 heat uptake above a long-term mean during our estimation period. It remains to be investigated if such an increased heat uptake during our estimation period, a potential under sampling in the *Levitus et al.* [2001] estimate or an unrealistic vertical diffusion in our result, could cause the discrepancy. The two top layers contribute about equally, while the deep part of the water column seems less important for this computation. Interestingly, the increase in our intermediate layer almost matches the *Levitus et al.* [2001] result, but the significance of this agreement is unclear. Note also that the increase comes to a halt in the top layer during the last ENSO event.

8. Summary and Conclusions

[62] A dynamically consistent time-dependent combination of a GCM and global data is used to estimate ocean transports of volume, heat and fresh water and to analyze their temporal changes. Emphasis is on estimating global oceanic cycles of heat storage and heat transport. Because the quality of the underlying flow estimates is limited by the present low resolution, the most important results here are the demonstration that these computations are feasible and can be used for quantitative estimates of important quantities that are not directly observable. The estimates will rapidly improve through the addition of new data, more complete model physics and higher resolution, but the present solution is probably among the best that can be done today. In particular, the analysis of the temporal variability of the transport properties is believed to be accurate, except for the variability owing to the unresolved eddy field and its effect on the large-scale.

[63] We have solved a fully time-dependent estimation problem, that includes the changing atmosphere and resulting surface transport fields as part of the solution. An important result from this study is that time-average transports of heat and freshwater estimated from this fully time-dependent circulation have converged with independent steady-flow estimates from box inversions over most parts of the world ocean, but especially in the southern hemisphere. *Marotzke and Willebrand* [1996] discuss earlier results obtained from box inversions and time-independent state estimations. Transport estimates do however, still differ substantially in the North Atlantic where our values are only one-half the best independent estimates.

[64] Although the low model resolution causes problems with estimates of the time average property transports, the patterns in the means are in encouraging quantitative agreement with independent previous estimates [e.g., *Wijffels et al.*, 1992; *Macdonald and Wunsch*, 1996; *Ganachaud and Wunsch*, 2000]. Equally important, we obtain an estimate of the ocean state that is in balance with simultaneous estimates of surface fluxes of momentum, heat and freshwater. The meridional heat transports esti-

mated from both transports within the model and from integrals of the surface heat fluxes are mostly consistent with the exception of the North Atlantic and within the rough error bars of Trenberth *et al.* [2001] in a comparison of NCEP, ECMWF, and COADS-derived values. A more complete discussion is provided by Stammer *et al.* (submitted manuscript, 2002b).

[65] Mean and time-varying volume transports for the entire three dimensional ocean circulation are estimated. Among the more striking results are the confirmation of previous findings of a mean circulation around Australia which involves a net volume transport of 11 Sv through the Indonesian Throughflow and the Mozambique Channel. In addition, we show that this flow regime exists on all timescales longer than one month-rendering the variability in the South Pacific strongly coupled to that of the Indian Ocean. Accordingly, the ACC shows a superposition of regional flow changes onto the global transports around Antarctica that are themselves dominated by a seasonal cycle. An estimated mean ACC transport of 124 Sv is in good agreement with previous direct observational findings.

[66] The temporal variability of oceanic heat transport, heat storage and atmospheric exchanges is complex, showing a dependence upon location, depth, and timescale as described above. Oceanic transports, storage, and air/sea exchange follow a complicated geographical pattern and exhibit variability on all accessible timescales. For the first time, we now have a prototype ocean data synthesis tool that provides a quantitative ocean transport analysis.

[67] The description given here of the oceanic heat budget remains tentative owing to remaining model/data shortcomings already described. However, we anticipate rapid improvement in all elements through model and data improvements now underway. Ongoing computations will complete a WOCE data synthesis including, in addition to the data used here, the WOCE hydrography, global XBT data sets, TAO temperature measurements, drifter surface velocities, PALACE and ARGO temperature and salinity profiles, etc. Computations are being carried out now on a nominal 1° grid and include mixed layer dynamics, the Gent-McWilliams mixing scheme and other improvements. Future large-scale oceanic observation programs will likely follow analysis methods similar to those used here.

[68] **Acknowledgments.** Computational support from the National Partnership for Computational Infrastructure (NPACI) and the National Center for Atmospheric Research (NCAR) is acknowledged. Supported in part through ONR (NOPP) ECCO grants N00014-99-1-1049 and N00014-99-1-1050, through NASA grant NAG5-7857, through NSF grant OCE 9730071 and through two contracts with the Jet Propulsion Laboratory (958125 and 1205624). This is a contribution of the Consortium for Estimating the Circulation and Climate of the Ocean (ECCO) funded by the National Oceanographic Partnership Program.

References

Arakawa, A., and V. R. Lamb, Computational design of the basic dynamical precesses of the UCLA General Circulation Model, in *Methods of Computational Physics*, vol. 17, pp. 174–265, Academic, San Diego, Calif., 1977.

Barnett, T., D. W. Pierce, and R. Schnur, Detection of anthropogenic climate change in the world's ocean, *Science*, 292, 270–274, 2001.

Bohren, C. F., and B. A. Albrecht, *Atmospheric Thermodynamics*, 402 pp., Oxford Univ. Press, New York, 1998.

Böning, C. W., and F. O. Bryan, Large-scale transport processes in high-resolution circulation models, in *The Warmwassersphere of the North Atlantic*, edited by W. Krauss, pp. 91–128, Gebrüder Bornträger, Stuttgart, Germany, 1996.

Carton, J. A., G. Chepurin, X. Cao, and B. S. Giese, A simple ocean data assimilation analysis of the global upper ocean 1950–1995, 1, Methodology, *J. Phys. Oceanogr.*, 30, 294–309, 2000a.

Carton, J. A., G. Chepurin, and X. Cao, A simple ocean data assimilation analysis of the global upper ocean 1950–1995, 2, Results, *J. Phys. Oceanogr.*, 30, 311–326, 2000b.

Döscher, R., C. W. Böning, and P. Herrmann, Response of circulation and heat transport in the North Atlantic to changes in thermocline forcing in northern latitudes: A model study, *J. Phys. Oceanogr.*, 24, 2306–2320, 1994.

Fukumori, I., R. Raghunath, and L.-L. Fu, Nature of global large-scale sea level variability in relation to atmospheric forcing: A modeling study, *J. Geophys. Res.*, 103, 5493–5512, 1998.

Ganachaud, A., and C. Wunsch, Oceanic meridional overturning circulation, mixing, bottom water formation rates and heat transport, *Nature*, 408, 453–456, 2000.

Godfrey, J. S., The effect of the Indonesian throughflow on ocean circulation and heat exchange with the atmosphere: A review, *J. Geophys. Res.*, 101, 12,217–12,238, 1996.

Gordon, A. L., Inter-ocean exchange of thermocline water, *J. Geophys. Res.*, 91, 5037–5046, 1986.

Holfort, J., and G. Siedler, The meridional oceanic transport of heat and nutrients in the South Atlantic, *J. Phys. Oceanogr.*, 31, 5–29, 2001.

Jayne, S. R., and J. Marotzke, The dynamics of ocean heat transport variability, *Rev. Geophys.*, 39, 385–412, 2001.

Kalnay, E., et al., The NCEP/NCAR re-analysis project, *Bull. Am. Meteorol. Soc.*, 77, 437–471, 1996.

Large, W. G., J. C. McWilliams, and S. C. Doney, Oceanic vertical mixing: A review and a model with nonlocal boundary layer parameterization, *Rev. Geophys.*, 32, 363–403, 1994.

Levitus, S., R. Burgett, and T. Boyer, *World Ocean Atlas 1994*, vol. 3, *Salinity*, NOAA Atlas NESDIS 3, U.S. Dep. of Commer., Washington, D. C., 1994a.

Levitus, S., R. Burgett, and T. Boyer, *World Ocean Atlas 1994*, vol. 4, *Temperature*, NOAA Atlas NESDIS 4, U.S. Dep. of Commer., Washington, D. C., 1994b.

Levitus, S., J. I. Antonov, J. Wang, T. L. Delworth, K. W. Dixon, and A. J. Broccoli, Anthropogenic warming of Earth's climate system, *Science*, 292, 267–270, 2001.

Macdonald, A. M., The global ocean circulation: A hydrographic estimate and regional analysis, *Prog. Oceanogr.*, 41, 281–382, 1998.

Macdonald, A. M., and C. Wunsch, An estimate of global ocean circulation and heat fluxes, *Nature*, 382, 436–439, 1996.

Marotzke, J., and J. Willebrand, The North Atlantic mean circulation: Combining data and dynamics, in *Warm Water Sphere of the North Atlantic Ocean*, edited by W. Krauss, pp. 159–193, Gebrüder Bornträger, Stuttgart, Germany, 1996.

Marotzke, J., R. Giering, Q. K. Zhang, D. Stammer, C. N. Hill, and T. Lee, Construction of the adjoint MIT ocean general circulation model and application to Atlantic heat transport sensitivity, newblock, *J. Geophys. Res.*, 104, 29,529–29,548, 1999.

Marshall, J., A. Adcroft, C. Hill, L. Perelman, and C. Heisey, A finite-volume, incompressible Navier–Stokes model for studies of the ocean on parallel computers, *J. Geophys.*, 5753–5766, 1997a.

Marshall, J., C. Hill, L. Perelman, and A. Adcroft, Hydrostatic, quasi-hydrostatic and non-hydrostatic ocean modeling, *J. Geophys.*, 5733–5752, 1997b.

McPhaden, M. J., et al., The tropical ocean global atmosphere observing system: A decade of progress, *J. Geophys. Res.*, 103, 14,169–14,240, 1998.

Nerem, R. S., D. P. Chambers, E. W. Leuliette, G. T. Mitchum, and B. S. Giese, Variations in global mean sea level associated with the 1997–1998 ENSO event: Implications for measuring long term sea level change, *Geophys. Res. Lett.*, 26, 3005–3008, 1999.

Nowlin, W. D., Jr., and J. M. Klinck, The physics of the Antarctic Circumpolar Current, *Rev. Geophys. Space Phys.*, 24, 469–491, 1986.

Peixoto, J. P., and A. H. Oort, The atmospheric branch of the hydrological cycle and climate, in *Variations in the Global Water Budget*, edited by A. Street-Perrott et al., pp. 5–65, D. Reidel, Norwell, Mass., 1983.

Ponte, R., D. Stammer, and C. Wunsch, Improved ocean angular momentum estimates using an ocean model constrained by large-scale data, *Geophys. Res. Lett.*, 28, 1775–1778, 2001.

Rintoul, S., South Atlantic inter-basin exchange, *J. Geophys. Res.*, 96, 2675–2692, 1991.

Roach, A. T., K. Aagaard, C. H. Pease, S. A. Salo, T. Weingartner, V. Pavlov, and M. Kulakov, Direct measurements of transport and water

- properties through the Bering Strait, *J. Geophys. Res.*, *100*, 18,443–18,457, 1995.
- Robbins, P. E., and J. M. Toole, The dissolved silica budget as a constraint on the meridional overturning circulation of the Indian Ocean, *Deep Sea Res., Part I*, *44*, 879–44,906, 1997.
- Roemmich, D., S. Hautala, and D. Rudnick, Northward abyssal transport through Samoan Passage and adjacent regions, *J. Geophys. Res.*, *101*, 14,039–14,055, 1996.
- Schneider, N., A. Miller, and D. W. Pierce, Anatomy of North Pacific Decadal Variability, *J. Clim.*, 586–605, 2002.
- Stammer, D., C. Wunsch, and R. Ponte, De-aliasing of global high frequency barotropic motions in altimeter observations, *Geophys. Res. Lett.*, *27*, 1175–1178, 2000.
- Stammer, D., C. Wunsch, R. Giering, C. Eckert, P. Heimbach, J. Marotzke, A. Adcroft, C. N. Hill, and J. Marshall, The global ocean circulation during 1992–1997, estimated from ocean observations and a general circulation model, *J. Geophys. Res.*, *107*(C9), 3118, doi:10.1029/2001JC000888, 2002a.
- Tierney, C., J. Wahr, F. Bryan, and V. Zlotnicki, Short-period oceanic circulation: Implications for satellite altimetry, *Geophys. Res. Lett.*, *27*, 1255–1258, 2000.
- Trenberth, K. E., J. M. Caron, and D. P. Sepaniak, The atmospheric energy budget and implications for surfaces fluxes and ocean heat transports, *Clim. Dyn.*, *17*, 259–276, 2001.
- Vranes, K., A. L. Gordon, and A. Ffield, The heat transport of the Indonesian throughflow and implications for the Indian Ocean Heat Budget, in *Physical Oceanography of the Indian Ocean During the WOCE Period*, *Deep Sea Res.*, edited by F. Schott, 2002 (in press).
- Warren, B. A., Approximating the energy transport across oceanic sections, *J. Geophys. Res.*, *104*, 7915–7919, 1999.
- White, W. B., and R. G. Peterson, An Antarctic circumpolar wave in surface pressure, wind, temperature and sea-ice extent, *Nature*, *380*, 699–702, 1996.
- Whitworth, T., Monitoring the transport of the Antarctic Circumpolar Current at Drake Passage, *J. Geophys. Res.*, *13*, 2045–2057, 1983.
- Wijffels, S. E., R. W. Schmitt, H. Bryden, and A. Stigebrand, Transport of freshwater by the ocean, *J. Phys. Oceanogr.*, *22*, 155–162, 1992.
- Wijffels, S. E., J. M. Toole, and R. Davis, Revisiting the South Pacific subtropical circulation: A synthesis of the World Ocean Circulation Experiment observations along 32°S, *J. Geophys. Res.*, *106*, 19,481–19,513, 2001.
-
- A. Adcroft, C. Eckert, P. Heimbach, C. N. Hill, J. Marshall, and C. Wunsch, Massachusetts Institute of Technology, Cambridge, MA 02139, USA.
- R. Giering, FastOpt, GBR, Hamburg, Germany.
- J. Marotzke, Southampton Oceanography Centre, University of Southampton, European Way, Southampton S01432H, UK.
- D. Stammer, Physical Oceanography Research Division, Scripps Institution of Oceanography, University of California, San Diego, Room 407, 8605 La Jolla Shores Drive, La Jolla, CA 92093-0230, USA. (dstammer@ucsd.edu)